Mechanics of Materials 197 (2024) 105107

Contents lists available at ScienceDirect

Mechanics of Materials

journal homepage: www.elsevier.com/locate/mechmat

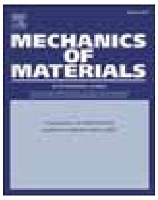

Research paper

# Medium entropy alloy-induced strong size dependence in the strengthening and shear instability of nanolayered metallic composites

Feng Qin [a,b], Kaiqing Dai [a], Junhua Hou [c], Wenjun Lu [c], Shaohua Chen [d], Jianjun Li [a,b,*]

[a] College of Mechanical and Electrical Engineering, Central South University, Changsha 410083, Hunan, PR China
[b] State Key Laboratory of Precision Manufacturing for Extreme Service Performance, Central South University, Changsha 410083, Hunan, PR China
[c] Department of Mechanical and Energy Engineering, Southern University of Science and Technology, Shenzhen 518055, PR China
[d] School of Aerospace Engineering, Beijing Institute of Technology, Beijing 100081, PR China

ARTICLE INFO

Handling Editor: J Molinari

*Keywords:*
Nanolayered metallic composites
Medium entropy alloys
Strengthening
Shear instability
Interfaces

ABSTRACT

Medium/high entropy alloys (M/HEAs)-based nanolayered metallic composites have attracted intensive scientific interests due to their superior mechanical properties. However, the shear instability of the M/HEAs-based composites is rarely studied and the underlying mechanism remains uncovered. A combination of theoretical analysis and nano/microindentation tests was conducted to investigate the size-dependent strengthening and shear instability of Cu/CrCoNi composites. The results show that the shear banding-induced instability of the composites exhibit a clear transition from layer interfaces-mediated kinking to grain boundaries-accommodated one at a critical layer thickness of 25 nm, which apparently differs from those in traditional M/HEAs-free composites. The sudden change in the deformation mode originates from the MEA-induced size-dependent microstructure transformation, i.e., from horizontally aligned layer interfaces at large layer thicknesses to vertically aligned grain boundaries at small ones. The size-dependent strengthening and plasticity can be respectively captured by the confined layer slip model and the proposed theoretical model.

## 1. Introduction

Extensive studies have shown that nanolayered metallic composites exhibit ultrahigh strength (Chen et al., 2018; Li et al., 2018a, 2022), significant ductility (Mara et al., 2008; Zhang et al., 2014), outstanding radiation damage tolerance (Huang et al., 2020; Li et al., 2012a), and increased wear resistance (Holmberg et al., 1998; Nasim et al., 2019), due to their high density of heterogeneous interfaces produced by the alternatively stacked constituent layers of different materials (Beyerlein et al., 2015; Li et al., 2018b). It has been unambiguously demonstrated that the strength and plasticity of various nanolayered metallic composites are highly tunable by varying the individual layer thickness ($h$) from around 100 nm to several nanometers or below (Cui et al., 2018; Dong et al., 2020, 2023; Gu et al., 2016; Nasim et al., 2020). It is found that the strength–layer thickness relation usually shows three different trends: (i) the strength always increases with the decrease of $h$ (down to 10 nm or below) (e.g. Cu/Zr (Niu et al., 2012), Ag/Nb (Cao et al., 2019a), Cu/W (Wen et al., 2007), Mo/Zr (Wu et al., 2018), Cu/Mo (Zhang et al., 2016), and Al/Nb (Fu et al., 2008)); (ii) the strength increases with the decrease of $h$ and then reaches a plateau when $h$ decreases to a critical value of around 10 nm (e.g. Ag/Ni (Li et al., 2016a), Cu/Cr (Misra et al., 1998)); (iii) the strength increases with the refining layers and then reaches a peak when $h$ decreases to a critical value of around 5 nm, after which the strength decreases with the further decrease of $h$ (e.g. Cu/Ni (Liu et al., 2011; Misra et al., 1998; Zhang et al., 2003), Ag/Fe (Li et al., 2016a), Cu/Nb (Misra et al., 2005a), Cu/Fe (Chen et al., 2012; Li et al., 2016a), Cu/V (Fu et al., 2008), and Cu/Co (Chen et al., 2015)). The size-dependent strengthening of the nanolayered metallic composites is attributed to the confined layer slip of single dislocation in the constituent crystalline layers, whereas the softening below the critical layer thickness results from the interface cutting by the dislocations due to the extremely confined space (Misra et al., 2005a).

In addition, the plasticity of nanolayered metallic composites has also been found to be strongly length-scale-dependent (Bhattacharyya et al., 2009; Cao et al., 2019a; Fan et al., 2017). The current works on nanolayered metallic composites are mainly based on microindentation, micropillar compression, and rolling experiments to evaluate the plastic

---

[*] Corresponding author. College of Mechanical and Electrical Engineering, and State Key Laboratory of Precision Manufacturing for Extreme Service Performance, Central South University, Changsha 410083, Hunan, PR China

*E-mail addresses:* mejjli@csu.edu.cn, jianjunli.mech@hotmail.com (J. Li).

https://doi.org/10.1016/j.mechmat.2024.105107
Received 10 November 2023; Received in revised form 24 July 2024; Accepted 30 July 2024

deformation (Li et al., 2017, 2020a; Misra et al., 2003; Qin et al., 2022). For instance, Li et al. (2009a) observed the plastic instability in the form of kinking-like shear banding in Cu/Au composites with $h = 50$ and 100 nm via microindentation experiments, while the cutting-like shear banding was witnessed at $h = 200$ and 500 nm. Another typical example is that Zhang and co-workers (Lei et al., 2012; Zhang et al., 2012) investigated Cu/Zr composites with $h$ spanning from 5 to 100 nm by micropillar compression tests and demonstrated that the Cu/Zr composites show totally different deformation behaviors with the decrease of $h$. At large $h$ (e.g., $h = 100$ nm), strong extrusion of the soft constituent phase (i.e., Cu layers) occurred, indicating the failure of the layered interfaces. However, the shear banding-induced strain localization dominates the deformation in the composites at smaller $h$ (e.g., $h = 10$ nm). Moreover, Misra et al. (Misra and Hoagland, 2007) systematically studied the plastic flow stability of Cu/Nb composites with layer thickness from nanometer scale to micrometer scale through room-temperature rolling experiments. It was found that as the initial layer thickness decreased, the deformation transformed from non-uniform reduction at a micrometer-scale initial layer thickness to through-thickness cracks at an initial layer thickness of less than 10 nm. To sum up, the cutting-like shear banding or inhomogeneous deformation is predominant in the crystalline/crystalline composites with large layer thickness ($h > 100$ nm), whereas sever shear localization or even the crack occurs in those with smaller layer thickness. The increased propensity of shear instability at smaller layer thickness is attributed to lower dislocation capacity and increasing mobility of interfaces and/or grain boundaries (GBs) (Lei et al., 2012; Li et al., 2009a).

Medium/high entropy alloys (M/HEAs) are a new class of materials which break down the traditional notions of base element (Cantor et al., 2004; Huang et al., 2023). Unlike traditional metallic alloys containing a base element and small amounts of alloying elements, HEAs are composed of five or more principal elements in an equimolar or near-equimolar composition, whereas MEAs involve 2–4 principal elements (Khallaf et al., 2022; Miracle and Senkov, 2017; Ye et al., 2016). So far, M/HEAs have received extensive attentions due to their outstanding strength (Sohn et al., 2019; Zou et al., 2015), ductility (Lei et al., 2018; Li et al., 2016b), work-hardening rate (Laplanche et al., 2018; Pacchioni, 2022), and damage tolerance at cryogenic temperatures (Ding et al., 2019). Recently, some attempts have been made to introduce M/HEAs into nanostructured composites, for instance, Cu/NbMoTaW (Zhao et al., 2018, 2020), Cu/$Ta_{50}Nb_{25}Mo_{25}$ (Jiang et al., 2021), Cu/FeCoCrNi (Zhao et al., 2021), etc. It has been uncovered that the strength and plasticity of the nanolayered metallic composites with M/HEAs as the constituent phases is also strongly dependent on the length scale.

However, due to the inherent characteristics of M/HEAs, some new phenomena that did not appear in the nanolayered composites composed of traditional metals/alloys were also discovered. For example, Zhao et al. (2018) reported that the hardness of Cu/NbMoTaW composites increased with the decrease of $h$ to a plateau value of 5.9 GPa at $h = 50$ nm, along with the transformation from Hall-Petch strengthening to interface barrier strengthening. In contrast, there is a significant difference in the critical thickness of hardness plateau between the Cu/NbMoTaW composites (at $h = 50$ nm) and the traditional nanolayered metallic composites (at a few nanometers). In addition, Zhao and co-workers (Zhao et al., 2019) prepared a series of Cu/FeCoCrNi composites and demonstrated that the hardness of Cu/FeCoCrNi composites increased continuously with the decrease of $h$ ($h = 5$–150 nm). Different from other bi-metal composites, the hard layers in the above M/HEA-based nanolayered composites provide more contributions to the plastic deformation than the soft ones. The fundamental reason lies in the fact that the soft nanotwinned Cu layers act as a source of dislocations and supply an abundance of dislocations that transmit across the coherent crystalline/crystalline interfaces to the hard FeCoCrNi layers, triggering their remarkable deformability. However, current studies are mainly focused on the size-dependent strengthening in the pure metal-M/HEAs nanolayered composites, but their plastic instability has been rarely investigated. Also, due to the very limited investigations on the mechanical behaviors of M/HEAs-based nanolayered composites, the underlying mechanisms of the size-dependent strengthening and plastic instability remain unrevealed.

In order to give a clearer and deeper understanding of the size dependence of the strengthening and deformability of the M/HEA-based nanolayered composites, a typical Cu/CrCoNi system was selected to combine the well-studied copper and equiatomic CrCoNi MEA (Gludovatz et al., 2016; Schneider et al., 2020) as the constituent phases in this paper. The size-dependent microstructure, hardness, shear instability, and underlying mechanisms of strengthening and deformation of the Cu/CrCoNi composites with $h = 2$–100 nm were systematically investigated by nano/microindentation tests. A theoretical model is developed to quantify the size-dependent shear instability of the composites. It is found that the microstructure of the MEA-based composite shows a strong size dependence, i.e., the horizontally aligned layer interfaces in the samples with large layer thicknesses ($h > 25$ nm) are replaced by the vertically aligned GBs in those with small ones. The microstructure transformation is unique in this MEA-based composite, which triggers a shift of deformation mode from the layer interfaces mediated-shear banding at large scales to the GBs-accommodated one at small scales. This finding is totally different from those observed in traditional M/HEA-free nanolayered composite systems (Li et al., 2009a,b), in which the shear instability is all undertaken by the layer interfaces including the cutting-like and kinking-like shear banding. Also, the as-prepared Cu/CrCoNi composites manifest the trend of “smaller is stronger” even when $h$ decreases to 2 nm, which can be well described by the refined confined layer slip (CLS) model. The article is organized as follows. Sect. 2 presents the experimental details. Sect. 3 shows the microstructures and mechanical behaviors of the designed Cu/CrCoNi composites, while Sect. 4 illustrates the underlying mechanisms of the size-dependent strengthening and shear instability. Finally, the conclusions are drawn in Sect. 5.

## 2. Experimental

Six Cu/CrCoNi nanolayered samples with $h$ ranging from 2 to 100 nm were deposited on Si (100) substrates by direct current magnetron sputtering at room temperature. Pure Cu (99.99%) and CrCoNi (99.9%) targets were used to produce the Cu/CrCoNi composites with the total thickness of 1.2 μm. Among all samples, the first layer on the wafer was Cu and the topmost one was CrCoNi. The deposition rates of Cu and CoCrNi were determined to be 0.1730 and 0.0874 nm $s^{-1}$, respectively. The pressure of the sputtering chamber was evacuated to less than $1.1 \times 10^{-4}$ Pa before deposition, and the Ar pressure was maintained as 0.5 Pa during sputtering process. The rotation speed of the substrate was set to be 30 rpm to enhance the uniformity of the microstructure of all sputtered samples.

X-ray diffraction (XRD, Bruker D8 Advance) analyses were utilized to characterize the crystallographic orientations of the Cu/CrCoNi composites. Transmission electron microscopy (TEM) and scanning TEM (STEM) were performed on Talos F200X G2 microscope equipped with energy dispersive spectroscopy (EDS) to investigate the internal microstructures and elemental distributions of the Cu/CrCoNi composites before and after deformation. The TEM foils were prepared by focused ion beam (FIB, FEI Helios Nanolab 600i) machining technique. The nano-hardness of all samples were measured using a Nanoindenter system (Keysight, Agilent G200) at room temperature under continuous stiffness measurement (CSM) mode. The maximum indentation depth was 350 nm, and 12 indentations were performed on each sample to improve the credibility of measurements. Among all the tests, the strain rate was set to be 0.05 $s^{-1}$. To investigate the shear deformation of the Cu/CrCoNi composites, the microindentation experiments were carried out by Shimadzu HMV-G20ST. All samples were indented under the load of 50 g, and the holding time was 5 s. Subsequently, the morphologies of indentation surface were characterized by using scanning electron microscopy (SEM, Tescan Mira 3).

## 3. Results

### 3.1. Microstructures of Cu/CrCoNi composites

The XRD patterns of all Cu/CrCoNi composites with $h$ spanning from 2 to 100 nm are shown in Fig. 1, indicating the crystal characteristics of all samples. The higher diffraction peaks located at 43.3° and lower peaks at 44.2° coincide with the (111) crystal plane of Cu (JCPDS No. 04–0836) and the (111) crystal plane of CrCoNi (Cao et al., 2019b), respectively, which proves that the as-prepared Cu/CrCoNi composites exhibit strong Cu (111) texture and relative weak CrCoNi (111) orientation. With the decrease of $h$, the intensity of two diffraction peaks decreases gradually, reaching the minimum at $h = 2$ nm. When $h$ decreases to 10 nm and below, the (111) peak of CrCoNi nearly disappears (Fig. 1, inset).

The STEM and the corresponding EDS images of the internal microstructures of the as-prepared Cu/CrCoNi composites with $h = 100$, 50, 25, 10, 5, and 2 nm are displayed in Fig. 2, presenting a clearly modulated layered structure and obvious contrast between two components in all samples. The distribution of Cu, Cr, Co, and Ni elements in all Cu/CrCoNi samples is uniform, with no obvious element segregation. Among them, due to the smaller layer thickness of two samples with $h =$ 5 and 2 nm, the distinction of element distribution between layers is not very clear (Fig. 2o and r). Note that the aligned columnar grained structure along the growth direction of samples can be observed when $h \leq 50$ nm. In addition, it is obvious that the interfaces between the Cu and CrCoNi layers are relatively flat when $h = 100$ nm (Fig. 2a–c), as well as the interfaces are wavy when $h = 50$, 25, 10, 5, and 2 nm (Fig. 2d–r). Specifically, the interfaces at the bottom (close to the Si substrate) are relatively flat when $h = 50$, 25, 10, 5, and 2 nm, while the interfaces at the top show a wavy structure, similar to the cases of reported results, such as Cu/Nb (Misra et al., 2005a,b) and Cu/$Fe_{50}Mn_{30}Co_{10}Cr_{10}$ (Zhao et al., 2022) composites. During the process of deposition, due to the lattice constant misfit between the film and the Si substrate, the strain energy gradually increases with the increase of the deposited atomic layer. In order to relax this energy, the growth mode of the film changes from layered growth to island growth after reaching a certain thickness, thus leading to wavy and broken interfaces (Nasim et al., 2019). When $h$ increases to 100 nm, the flat deposited layers are formed due to the coalescence of islands during sputtering (Fig. 2a).

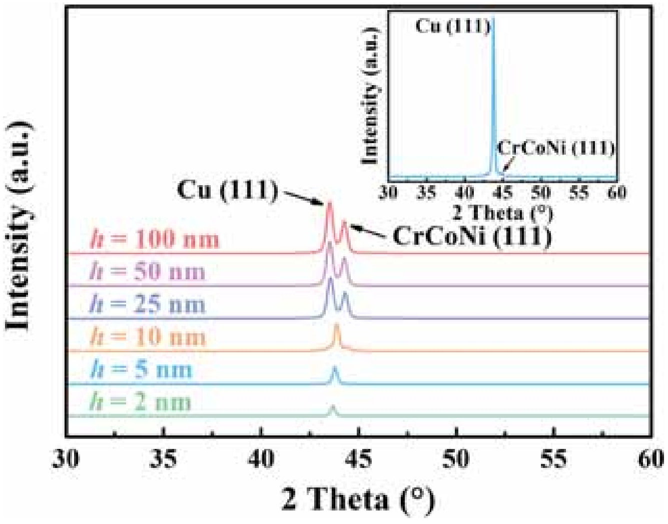

**Fig. 1.** XRD patterns of the Cu/CrCoNi composites with different layer thicknesses. The inset shows the magnified XRD pattern of the Cu/CrCoNi composite with $h = 5$ nm.

To further explore the internal microstructures of the Cu/CrCoNi composites, TEM is employed. As shown in Fig. 3, the clear modulated layered structure of the Cu/CrCoNi composites with various $h$ and the columnar grained structure of the Cu/CrCoNi composites with $h \leq 25$ nm can be witnessed, which is well in accordance with the aforementioned STEM and EDS results in Fig. 2. In addition, the bright-field TEM images (Fig. 3a–c, g, i and k) further show the column morphology of the composites. The SAED pattern (Fig. 3b) and FFT patterns (insets in Fig. 3c–g, i and l) reveal the twinned orientations either in CrCoNi or Cu layers. The high-resolution TEM (HRTEM) views (Fig. 3b–d, f, h, j, and l) demonstrate that the orientation between the Cu and CrCoNi layers depends on the specific layer thickness. At large layer thickness, e.g., $h = 50$ nm (Fig. 3d), the Cu–CrCoNi interface shows a {111}<110>Cu//{111}<110>CrCoNi cube-on-cube orientation, such that the interface plane is {111}Cu//{111}CrCoNi, while {111}Cu//{111}CrCoNi hetero-twin interfaces with atomic steps are observed in the samples with h of 25 nm (Fig. 3f) and 10 nm (Fig. 3h). Different from the cube-on-cube Cu–CrCoNi interface, the slip systems across the hetero-twin interface exhibit a mirror symmetry orientation relationship between the Cu and CrCoNi layers (Fig. 3f and h). In the case of small layer thickness (5 and 2 nm), there are coexistence of {111}<110>Cu//{111}<110>CrCoNi interface with parallel slip systems and {111}<110>Cu//{0002}<11–20>CrCoNi incoherent interface due to formation of hexagonal close-packed (hcp) CrCoNi near the interface, as shown in Fig. 3j and l.

The TEM analysis (Fig. 3d–f, h, j, l) shows that the interfaces between Cu and CrCoNi layers are typical sharp interfaces (with low-index planes and tend to be atomically flat), which is distinguished from the facet interface as well as the 3D interface. The sharp/flat interfaces are common in nanolayered composites as prepared by physical vapor deposition techniques, such as magnetron sputtering (Zheng et al., 2014) and electron beam evaporation (Li et al., 2012b). The facet interface results from joining two crystals at crystallographic planes that are serrated (Kang et al., 2012), which is usually formed by severe plastic deformation, e.g., accumulative roll bonding (Zheng et al., 2013). The 3D interfaces are one kind of hetero-phase interfaces with a certain thickness, which are chemically, crystallographically, and/or topologically distinct from their constituent phases in three dimensions as proposed by Chen et al. (2020).

It has been reported that the formation of the nanotwins in the sputtered samples is determined by two critical parameters, i.e., the stacking fault energy (SFE) (Bajpai et al., 2022) and the deposition rate of the materials (Zhang et al., 2004). The lower the SFE or the higher the deposition rate, the bigger the possibility of nanotwin nucleation (Zhang et al., 2004). It is known that CrCoNi has low SFE ranging from 1.4 to 57 mJ $m^{-2}$ (Li et al., 2019), and the deposition rates of the Cu and CoCrNi targets in this experiment are relatively large (0.1730 and 0.0874 nm $s^{-1}$, respectively). Therefore, a large number of nanotwins were generated during the deposition process. Note that parallel stacking faults (SFs) on basal planes and twins are mostly observed in CrCoNi layers whereas randomly observed in several Cu layers (Fig. 3d–f, h, j, l). Particularly, the SFs are usually localized near the interfaces.

Then, the grain size ($d$) in both Cu and CrCoNi layers are measured from the cross-sectional TEM views, as shown in Fig. 4. The average grain sizes in the Cu layers for the Cu/CrCoNi composites with $h = 100$, 50, 25, 10, 5, and 2 nm are 67.4 ± 14.3 nm, 46.2 ± 11.7 nm, 36.3 ± 10.9 nm, 30.3 ± 7.0 nm, 27.9 ± 5.5 nm, and 27.4 ± 4.9 nm (Fig. 4a–f), respectively. With the decrease of $h$, the grain size in the Cu layers decreases gradually. Similar to the case of the Cu layers, the grain size in the CrCoNi layers decreases from 63.7 ± 14.2 nm to 27.0 ± 5.6 nm with the decrease of $h$ (Fig. 4g–l). The aforementioned results prove that the grain size in the Cu/CrCoNi composites strongly depends on the layer thickness, and the grain size is smaller than the layer thickness for the samples with $h = 100$ and 50 nm, but is larger than the layer thickness for the samples with $h = 25$, 10, 5, and 2 nm. Moreover, the actual thicknesses of the Cu and CrCoNi layers are measured to be 95.9 ± 7.3

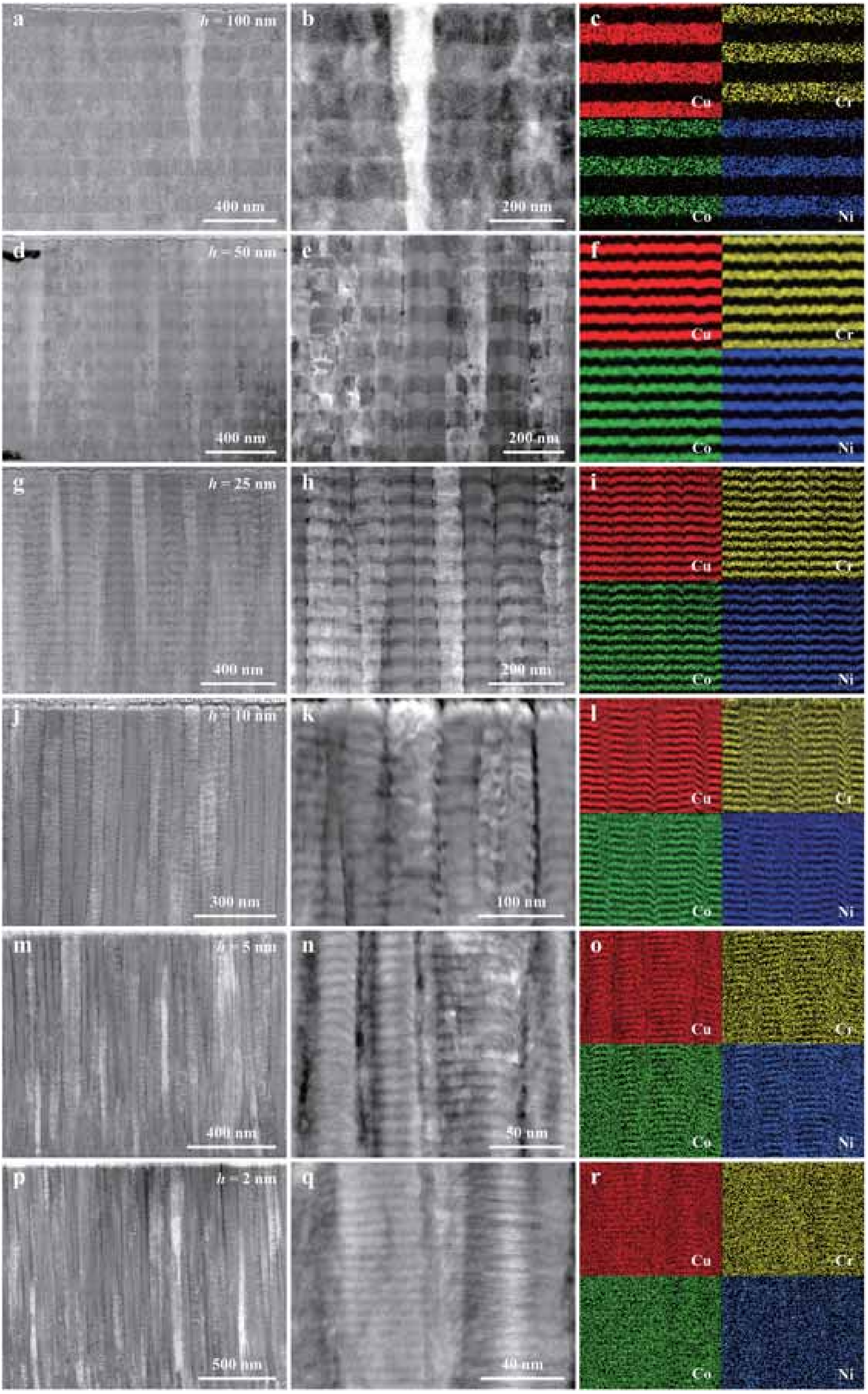

**Fig. 2.** STEM images and the corresponding EDS mapping images of the Cu/CrCoNi composites with $h$ = (a–c) 100, (d–f) 50, (g–i) 25, (j–l) 10, (m–o) 5, and (p–r) 2 nm, respectively.

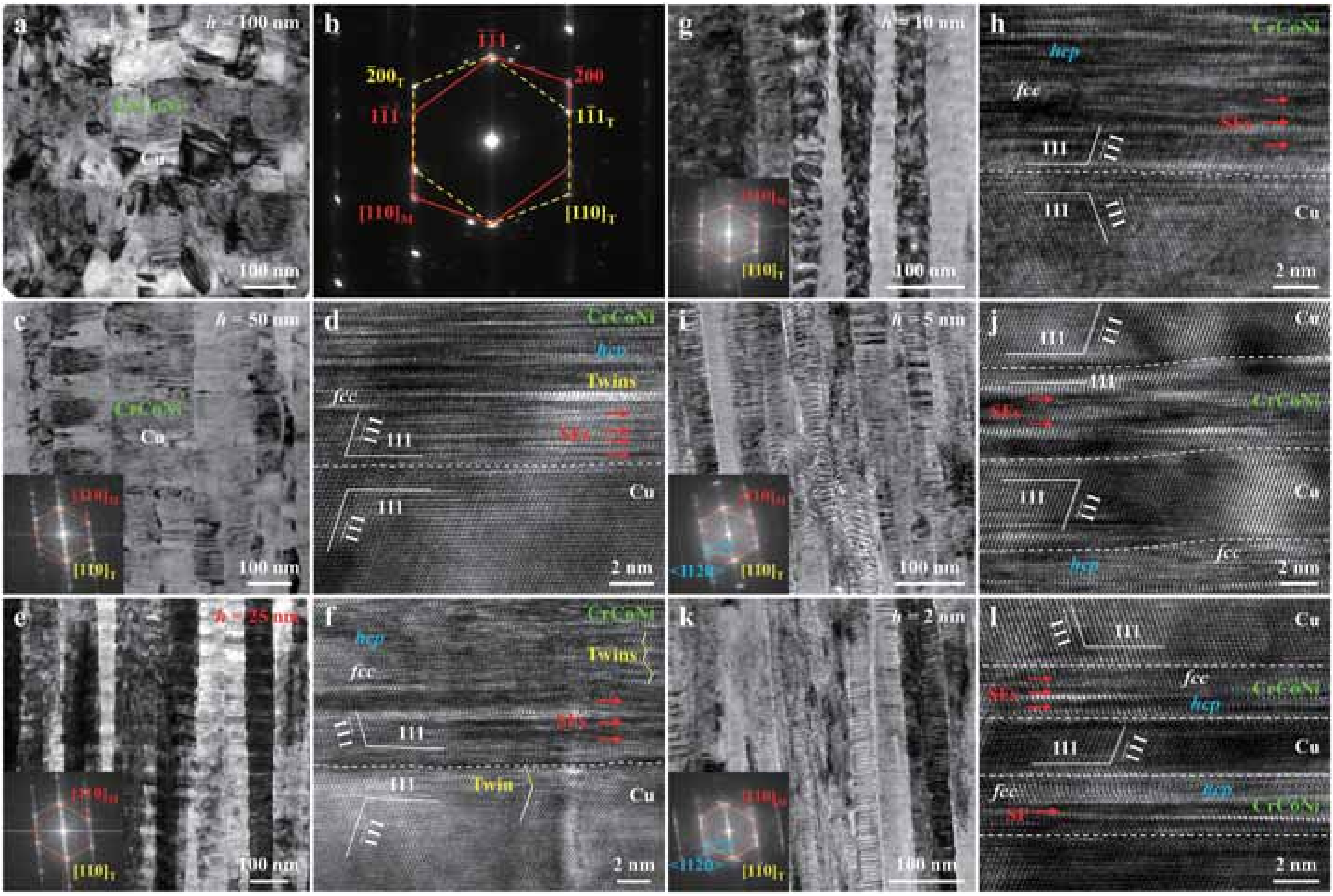

**Fig. 3.** Cross-sectional microstructures of the Cu/CrCoNi composites. (a) Bright-field TEM image of the composite with $h$ of 100 nm. (b) Representative SAED pattern in (a) taken along [110] zone axis, showing the twinned orientations either in CrCoNi or Cu layers. (c–l) TEM images and the corresponding HRTEM images of the composites with $h = 50$ (c, d), 25 (e, f), 10 (g, h), 5 (i, j), and 2 nm (k, l), respectively. Insets in (c, e, g, i, k) are the corresponding FFT patterns.

nm and 97.6 ± 7.8 nm for $h = 100$ nm, 56.1 ± 2.4 nm and 55.0 ± 1.5 nm for $h = 50$ nm, 27.2 ± 3.0 nm and 22.9 ± 2.8 nm for $h = 25$ nm, 10.5 ± 0.7 nm and 7.6 ± 0.7 nm for $h = 10$ nm, 4.8 ± 0.6 nm and 4.4 ± 0.4 nm for $h = 5$ nm, as well as 2.3 ± 0.3 nm and 2.1 ± 0.2 nm for $h = 2$ nm, respectively. It can be noted that $d < h$ as $h > 25$ nm, whereas $d > h$ when $h \leq 25$ nm, as summarized in Fig. 5.

### 3.2. Mechanical behaviors of Cu/CrCoNi composites

#### 3.2.1. The hardness of Cu/CrCoNi composites

The hardness and elastic modulus of the Cu/CrCoNi composites were measured by nanoindentation tests, as plotted in Fig. 6. The hardness–indentation depth curves of six samples (Fig. 6a) show that the hardness ($H$) values reach a plateau at the indentation depth of 120–200 nm. With the further increase of indentation depth, the hardness values increase gradually on the basis of the plateau values due to the substrate effect. As a result, the average hardness within the indentation depth of 10%–15% of total thickness (corresponding to 120–180 nm) is adopted as the intrinsic hardness values for each sample to eliminate the substrate effect. The variation of hardness of the Cu/CrCoNi composites with the layer thickness is shown in Fig. 6b. Of note, the hardness increases monotonically with reducing $h$, reaching a maximum value of 7.8 ± 0.2 GPa at $h = 2$ nm, which is far different from the previously reported face-centered cubic (*fcc*)/*fcc* bi-metal composites. In some cases of *fcc*/*fcc* bi-metal composites, softening can be observed at extremely small layer thickness ($h < 5$ nm), such as Cu/Ni (Liu et al., 2011), Ag/Ni (Yu et al., 2013), and Cu/Co (Liu et al., 2013) composites, while in others, the hardness reaches a plateau when $h < 25$ nm, such as Cu/330 stainless steel (Zhang et al., 2004) and Cu/Fe (Chen et al., 2012) composites. In order to more clearly describe the strengthening effect of the layered structure, the predicted hardness based on the rule of mixture (ROM) is also calculated as follows:

$$H_{\mathrm{ROM}} = f_{\mathrm{Cu}} H_{\mathrm{Cu}} + f_{\mathrm{CrCoNi}} H_{\mathrm{CrCoNi}} \tag{1}$$

where $H_{\mathrm{Cu}} = 3.0$ GPa, $H_{\mathrm{CrCoNi}} = 7.6$ GPa (Cao et al., 2019b), and $f_{\mathrm{Cu}}$ and $f_{\mathrm{CrCoNi}}$ are the volume fractions of the Cu and CrCoNi layers, respectively. The calculations show that the hardness of all Cu/CrCoNi samples is higher than $H_{\mathrm{ROM}}$ (5.3 GPa) except for the sample with $h = 100$ nm. Notably, the maximum hardness is even higher than that of the hardest one, i.e., CrCoNi, similar to the cases of previously reported *fcc*/*fcc* Cu/Ni (Liu et al., 2011) and Cu/FeCoCrNi (Zhao et al., 2019) composites. In contrast, the data of elastic modulus–indentation depth curves (Fig. 6c) have higher discrete degree. The elastic modulus ($E$) data with the indentation depth of 15% of entire thickness are chosen to characterize the intrinsic elastic modulus of each sample. As presented in Fig. 6d, the elastic modulus remains almost constant with $h$ varying from 50 to 5 nm, as well as the elastic modulus sharply increases when $h$ decreases from 100 to 50 nm and $h < 5$ nm.

#### 3.2.2. The shear instability of Cu/CrCoNi composites

The indentation morphologies of the Cu/CrCoNi composites are investigated by SEM, as depicted by Fig. 7. The results show that almost all samples (except the sample with $h = 100$ nm) share the same shear banding behavior as indicated by well-shaped circular shear bands (SBs), which are denoted by the white arrows in the indentation areas

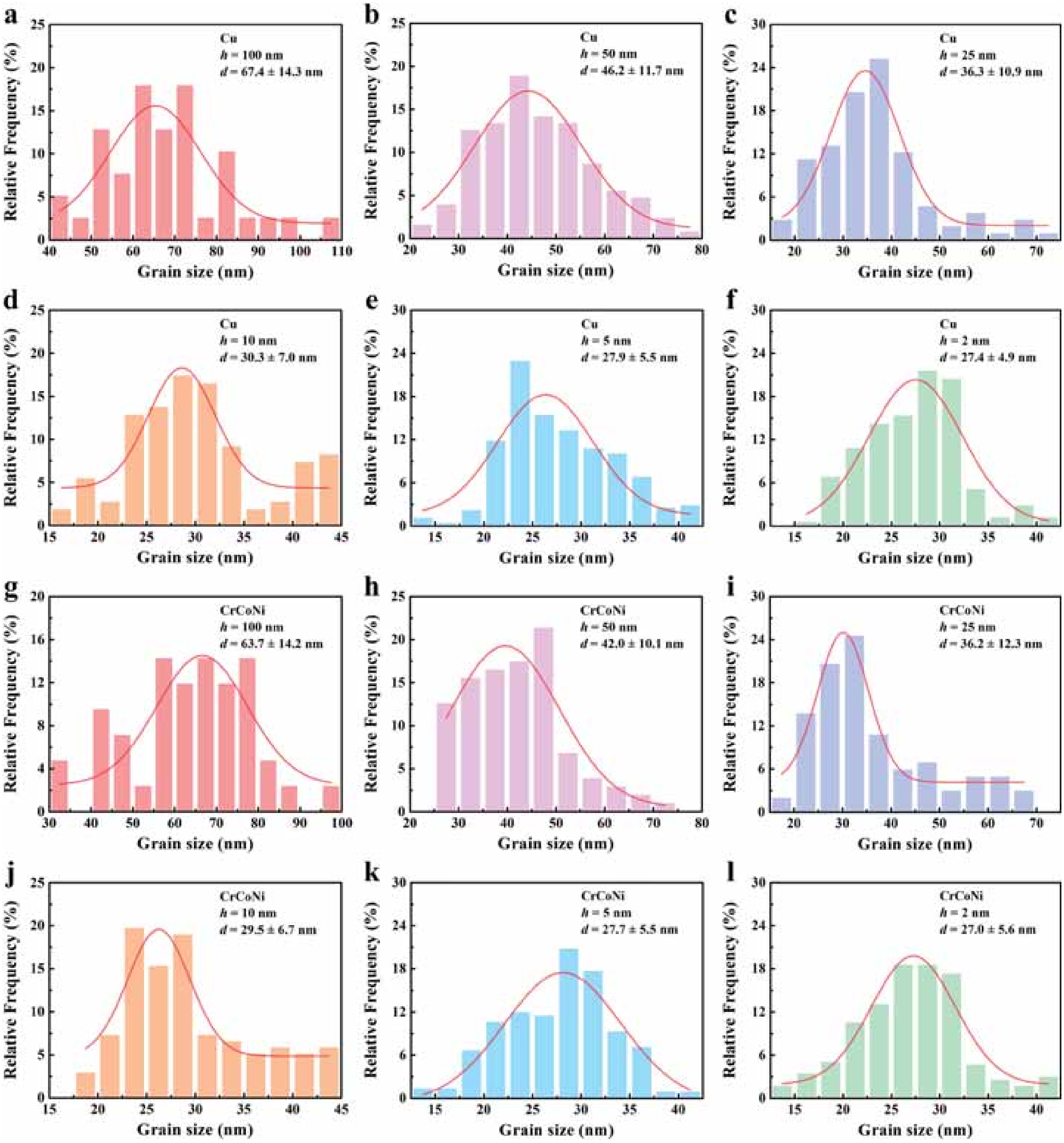

**Fig. 4.** Histograms of grain size in the (a–f) Cu and (g–l) CrCoNi layers for the Cu/CrCoNi composites with $h = 100$, 50, 25, 10, 5, and 2 nm, respectively.

(Fig. 7a–e). In contrast, the sample with $h = 100$ nm only shows slight pile-ups in the indentation region (Fig. 7f). Meanwhile, some micro-cracks can be observed at the edges of the SBs in the samples with $h$ less than 100 nm as denoted by the orange arrows in Fig. 7a–e, which is otherwise absent in the sample with $h = 100$ nm (Fig. 7f). These findings suggest that much better plasticity and toughness have been gained in the sample with $h = 100$ nm as compared with the other counterparts. Moreover, the sample with $h = 50$ nm possesses a slightly smaller number of SBs (i.e., 8) than those with $h = 2$–25 nm (i.e., 9–11), which also indicates a better plasticity in the former than in the latter.

In order to further elucidate the shear instability of the designed Cu/CrCoNi composites, the cross-sectional TEM lamellas were prepared from the residual indentations with $h = 100$, 50, 25, 10, 5, and 2 nm. Fig. 8a presents a SEM view of the indentation surface of the Cu/CrCoNi composite with $h = 100$ nm, and the corresponding cross-sectional microstructure is investigated by TEM. As shown in Fig. 8b, the Cu and CrCoNi layers are represented by the bright and dark layers, respectively, which is also confirmed by the corresponding EDS analysis

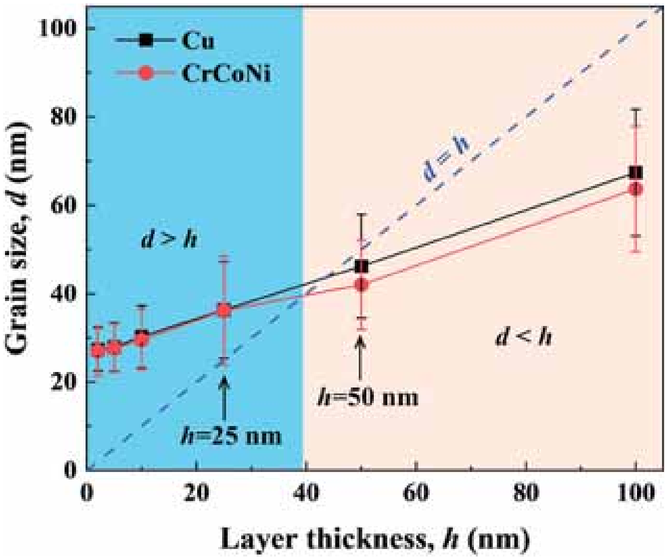

**Fig. 5.** The relationship between the measured layer thickness ($h$) and grain size ($d$) of the Cu/CrCoNi composites.

of Cu (Fig. 8c). Obviously, one long SB is formed to kink all constituent layers of the Cu/CrCoNi composite with $h = 100$ nm as marked by the white dashed lines. By comparison, three typical kinking-like SBs appear in the Cu/CrCoNi composite with $h = 50$ nm (Fig. 8d–f) under the same microindentation conditions. According to the distance between the SBs and microindenter from near to far, the three SBs are marked as 50-SB1, 50-SB2, and 50-SB3, respectively. Among them, the 50-SB1 is not visible in SEM image of the indentation area because of its small shear displacement. The above findings clearly show that the shear banding of the Cu/CrCoNi composites with $h = 100$ and 50 nm is produced by the cooperative kinking of all horizontal layered interfaces, although their indentation surfaces show different morphologies.

However, it is intriguing to find that the Cu/CrCoNi composites with $h = 25$, 10, 5, and 2 nm exhibit totally distinct shear banding behavior, in which the kinking-like shear banding is mediated by the vertically aligned GBs of all columnar grains (Figs. 9 and 10), instead of the horizontally aligned layered interfaces in the Cu/CrCoNi composites with $h = 100$ and 50 nm. Also, the original continuous constituent layers in the top are separated by the SBs (Fig. 9d, 10d and 10e), which result from the kinking of the vertical GBs. The above difference in shear banding behavior might come from the fact that the columnar GBs are more aligned than the wavy layered interfaces in the Cu/CrCoNi composites with $h = 25$, 10, 5, and 2 nm, which is otherwise reversed in the Cu/CrCoNi composites with $h = 100$ and 50 nm (Fig. 2), because the cooperative kinking-like shear banding favors a more aligned interface structure. At small layer thicknesses ($h = 25$, 10, 5, and 2 nm), the aligned columnar grains are more involved in the plastic deformation.

To quantify the shear instability and to predict the shear banding direction of the Cu/CrCoNi composites with different layer thicknesses, here a theoretical model is developed based on the pure shear stress state in the shear banding region (Figs. 11 and 12). Fig. 11a and b represent the model of kinking-like SBs mediated by the layered interfaces as observed in the samples with $h = 100$ and 50 nm, while the model of kinking-like SBs dominated by the vertically aligned GBs observed in the samples with $h = 25$, 10, 5, and 2 nm is depicted in Fig. 11c and d. The SB angle ($\alpha$) of a given SB is defined as the angle between the original layered interfaces (when $h = 50$ and 100 nm, Fig. 11a) or the aligned GBs (when $h = 25$, 10, 5, and 2 nm, Fig. 11c) and the SB, as well as $\varphi$ denotes the kinking angle between the kinking interfaces and the original ones. It is assumed that the regions of SBs are subjected to pure shear stress state. Hence, the shear strain ($\gamma$) of the $i$-th layer within a given SB in all samples with different layer thicknesses can be expressed by the same formula, which is calculated as the change of the right angle in the microelement before and after deformation based on the geometries in Fig. 11b and d:

$$\gamma_i = \beta - \beta^{`} = \varphi_i + \alpha - \frac{\pi}{2} \tag{2}$$

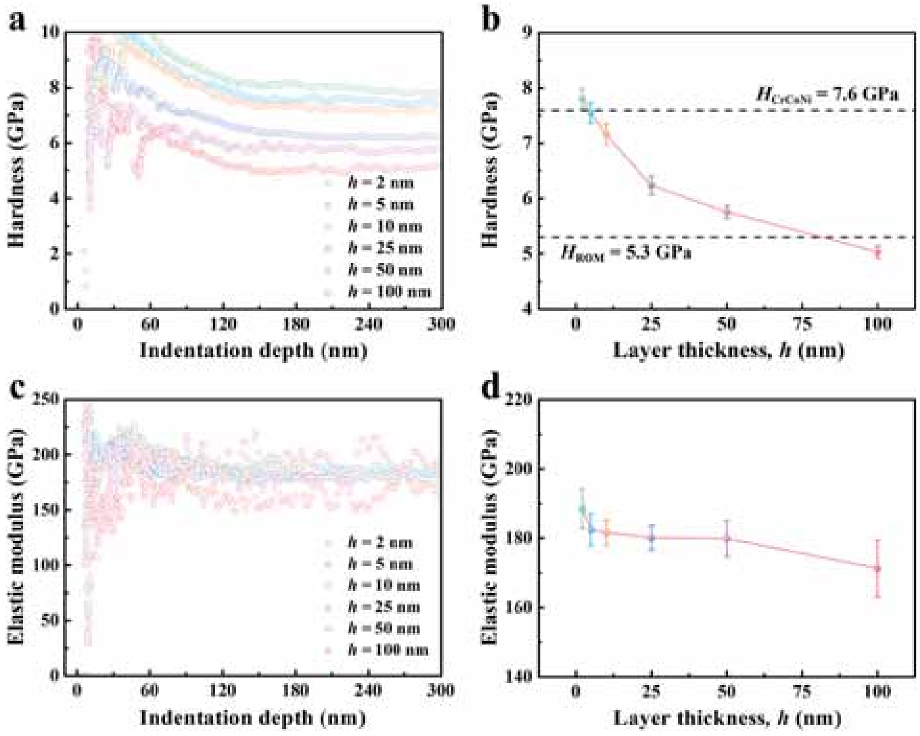

**Fig. 6.** (a) The typical hardness–indentation depth curves and (b) the dependence of hardness on the layer thickness of the Cu/CrCoNi composites. (c) The typical elastic modulus–indentation depth curves and (d) the dependence of elastic modulus on the layer thickness of the Cu/CrCoNi composites.

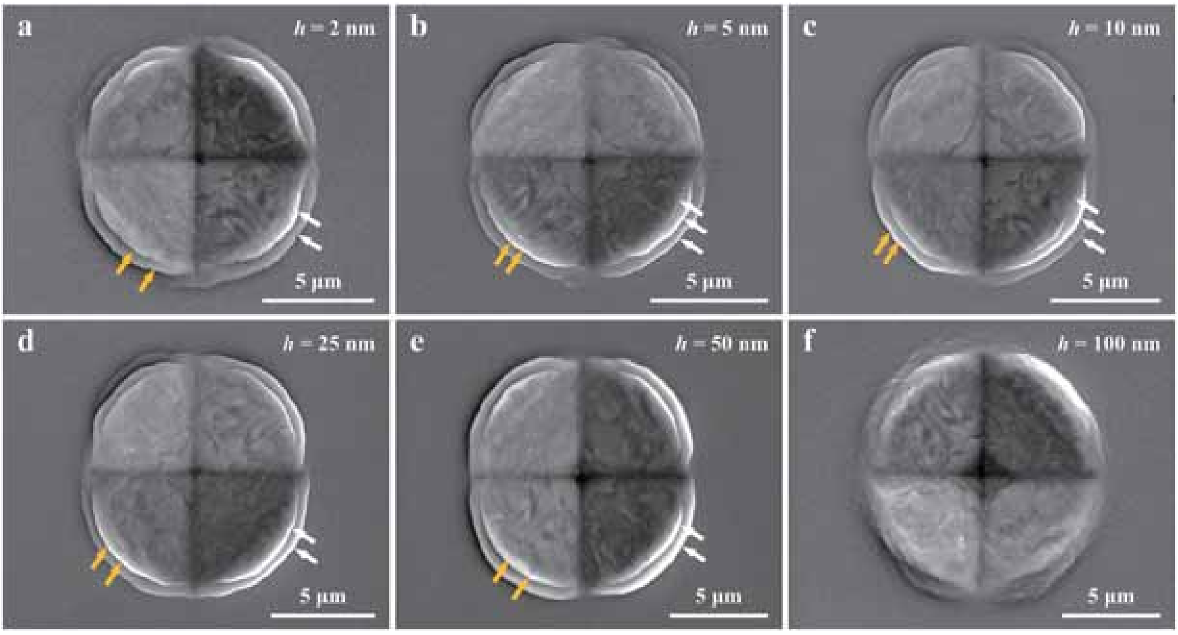

**Fig. 7.** (a–f) SEM images of the indentations of the Cu/CrCoNi composites with $h$ ranging from 2 to 100 nm. The white and orange arrows point to well-shaped circular SBs and microcracks, respectively. (For interpretation of the references to colour in this figure legend, the reader is referred to the Web version of this article.)

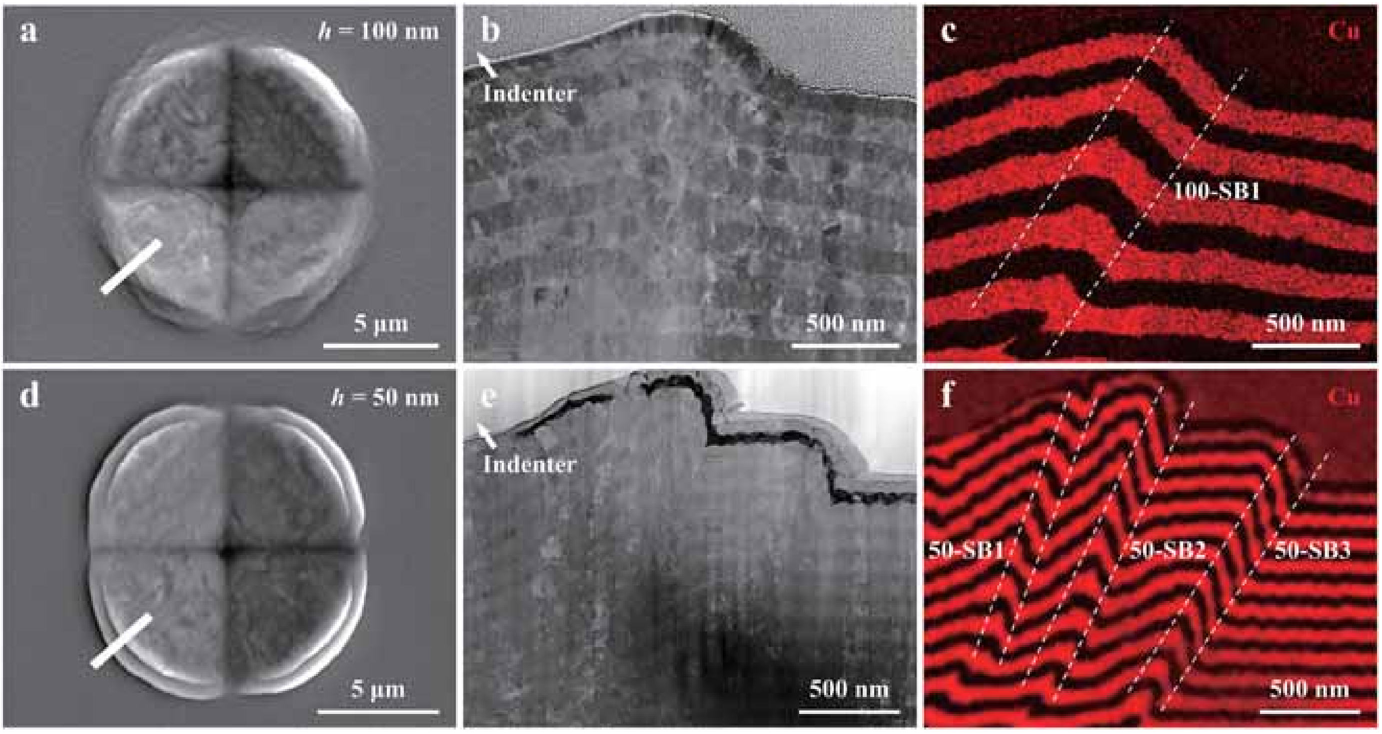

**Fig. 8.** (a, d) SEM images, the corresponding cross-sectional (b) TEM image, (e) high-angle annular dark-field STEM image, and (c, f) EDS mapping images of the indentations of the Cu/CrCoNi composites with $h$ = 100 and 50 nm, respectively. The white solid lines in (a, d) designate where the cross-sectional lamellae are extracted. The positions of the indenter tips are arrowed in (b, e). The regions of SBs are indicated by white dashed lines in (c, f).

where $i$ represents the number of the constituent layers from bottom to top. Because the columnar GBs huddle together within SBs for the Cu/CrCoNi composite with $h = 25$ and 10 nm, the parameter $\varphi_i$ of each layer cannot be measured clearly. As a result, the kink of vertical columnar GBs is considered as a whole and only one value of $\gamma$ in each SB is chosen to characterize the shear deformation for the Cu/CrCoNi composites with $h = 25$ and 10 nm. Since $\varphi$ is in the range of $[0, \pi - \alpha]$, the maximum value of $\gamma$ is $\pi/2$.

In addition to the shear strain parameter, a strain localization parameter can also be defined for each constituent layer in a given SB by dividing the shear displacement ($h_i$) by SB width ($w_{\mathrm{SB}}$):

$$\xi_i = \frac{h_i}{w_{\mathrm{SB}}} \tag{3}$$

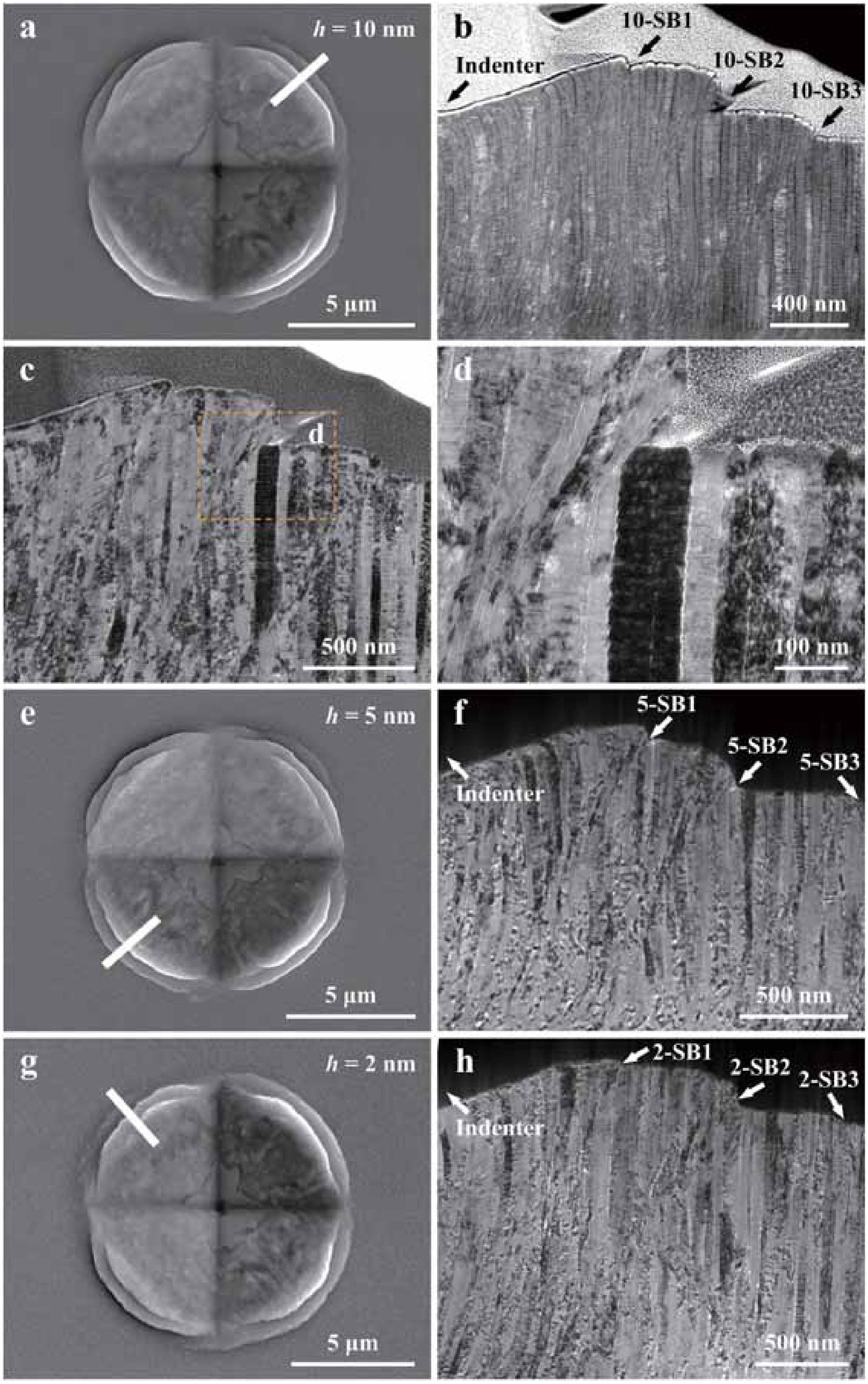

**Fig. 9.** (a, e, g) SEM images, the corresponding cross-sectional (b, f, h) STEM images, and (c, d) bright-field STEM images of the indentations of the Cu/CrCoNi composites with $h = 10$, 5, and 2 nm. The white solid lines in (a, e, g) designate where the cross-sectional lamellae were extracted. (d) is the magnified view of the boxed region in (c). The positions of the indenter tips and the regions of SBs are indicated by arrows in (b, f, h).

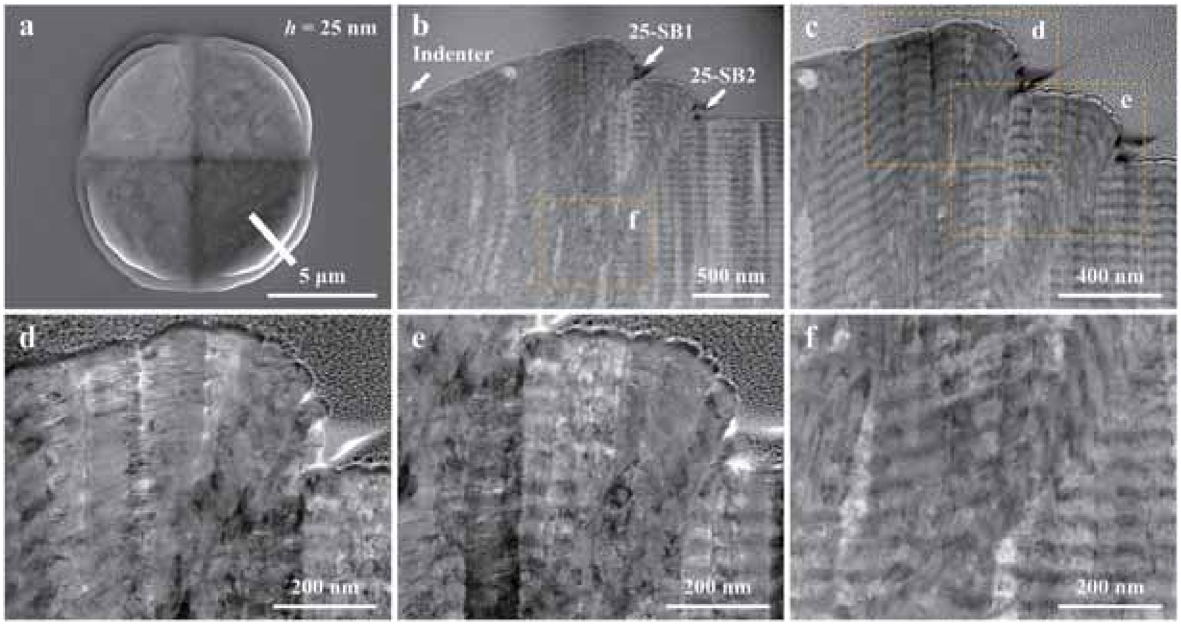

**Fig. 10.** (a) SEM image, the corresponding cross-sectional (b, c, f) STEM images, and (d, e) dark-field STEM images of the indentation of the Cu/CrCoNi composite with $h = 25$ nm. The white solid line in (a) designates where the cross-sectional lamella was extracted. (d, e, f) are the magnified views of the boxed regions in (b, c), respectively. The position of the indenter tip and the regions of SBs are indicated by arrows in (b).

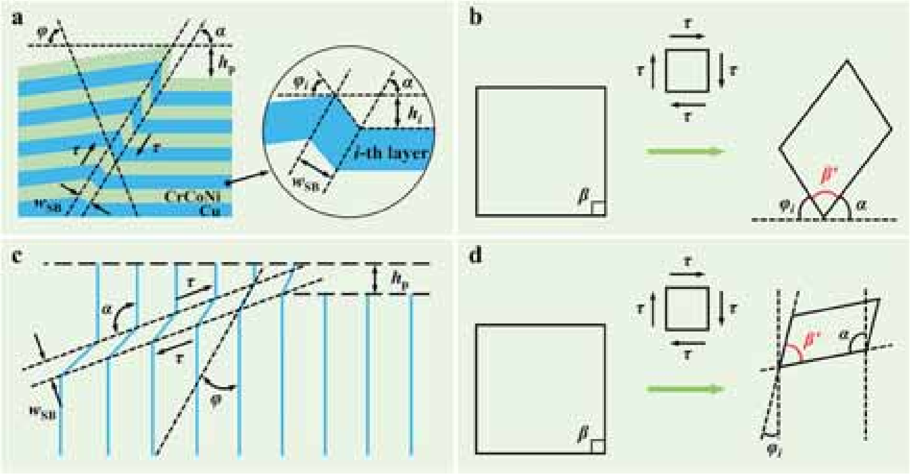

**Fig. 11.** Schematic diagrams for (a) the geometric model of kinking-like SBs mediated by the horizontal layered interfaces and (b) the corresponding microelement deformation within the given SB under pure shear stress state in the Cu/CrCoNi composites with $h = 100$ and 50 nm. Schematic diagrams for (c) the geometric model of kinking-like SBs mediated by the vertically aligned columnar GBs and (d) the corresponding microelement deformation within the given SB under pure shear stress state in the Cu/CrCoNi composites with $h = 25$, 10, 5, and 2 nm. In the above schematic diagrams, $\beta$ and $\beta'$ are the angles before and after deformation, respectively. The magnified image in (a) shows the geometric model details of the $i$-th layer, where $\varphi_i$ and $h_i$ denote the interface kink angle and shear displacement induced by the SB of the $i$-th layer, respectively.

By a simple algebra derivation based on the above geometry (Fig. 11a), the strain localization parameter can be given as the function of the kinking angle and the SB angle, i.e.,

$$\xi_i = \frac{\sin \varphi_i}{\sin(\alpha + \varphi_i)} \tag{4}$$

Eq. (4) shows that $\xi_i$ is positively related to the interface kink angle considering that $\alpha$ is constant for a given SB, similar to the $\gamma_i - \varphi_i$ relation given in Eq. (2). As a result, in addition to the shear strain $\gamma_i$, the strain localization parameter $\xi_i$ can also be employed to quantify the shear instability-induced strain localization for each layer in a given SB. Consider a given SB as an ensemble, its corresponding $\xi_\mathrm{p}$ can be expressed as:

$$\xi_\mathrm{p} = \frac{h_\mathrm{p}}{w_\mathrm{SB}} \tag{5}$$

in which $h_\mathrm{p}$ is the surface shear displacement in a given SB (Fig. 11a and c). Due to the severe shear instability of the Cu/CrCoNi composites with $h = 5$ and 2 nm, it is difficult to accurately measure their $w_\mathrm{SB}$ and $\varphi$. Therefore, the shear instability of the two samples is not quantitatively analyzed.

The measured values of $\alpha$, $h_\mathrm{p}$, and $w_\mathrm{SB}$ of the Cu/CrCoNi composites with $h = 100$, 50, 25, and 10 nm based on Figs. 8–10 are listed in Table 1. It can be seen from Table 1 that the average $w_\mathrm{SB}$ of several SBs decreases with the decrease of $h$. A similar relationship between $w_\mathrm{SB}$ and $h$ has been reported in Cu/Au composites (Li et al., 2010b; Zhang et al., 2006), i.e.,

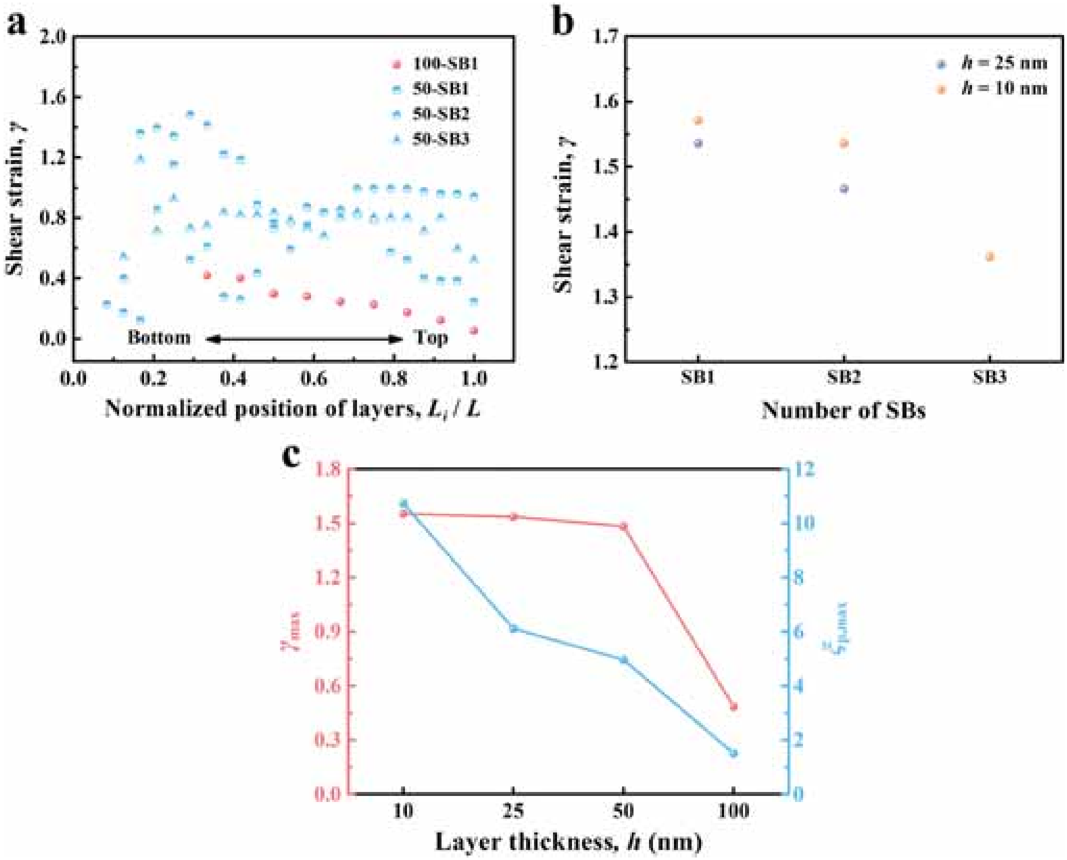

**Fig. 12.** (a, b) The calculated $\gamma$ within different SBs and (c) the corresponding calculated $\gamma_{max}$ and $\xi_{p,max}$ of the Cu/CrCoNi samples with $h = 100$, 50, 25, and 10 nm, respectively. $L_i/L$ denotes the normalized position of the constituent layers in each sample, where $L_i$ is the position of the $i$-th layer from bottom to top and $L$ is the total thickness of each sample.

**Table 1**
Summary of $\alpha$, $w_{SB}$, and $h_p$ for the Cu/CrCoNi composites with $h = 100$, 50, 25, and 10 nm.

| SB | $\alpha$ (°) | $w_{SB}$ (nm) | $h_p$ (nm) |
|---|---|---|---|
| 100-SB1 | 59 | 271 | 407 |
| 50-SB1 | 71 | 103 | 495 |
| 50-SB2 | 70 | 119 | 591 |
| 50-SB3 | 61 | 167 | 269 |
| 25-SB1 | 155 | 81 | 495 |
| 25-SB2 | 149 | 83 | 203 |
| 10-SB1 | 158 | 38 | 408 |
| 10-SB2 | 154 | 86 | 237 |
| 10-SB3 | 144 | 24 | 38 |

the $w_{SB}$ monotonically decreases as $h$ decreases. Different from the Cu/Au and Cu/CrCoNi composites, the $w_{SB}$ of Cu/amorphous CuNb composites shows a trend of first decreasing and then increasing with the decrease of $h$ (Qin et al., 2024). After summarizing relevant literature and the experimental data in this paper, it is found that the changing trend of $w_{SB}$ with $h$ is negatively correlated with the changing trend of degree of shear instability with $h$. That is, the decrease of $w_{SB}$ indicates that plastic deformation is localized in narrower SBs, implying that the shear instability becomes more severe. However, it is not comprehensive to directly judge the degree of shear instability with different $h$ just by the changing trend of $w_{SB}$ with $h$, which should be further accurately quantified according to the afore-mentioned $\xi_p$.

The value of $\alpha$ for 100-SB1 is measured to be 59° when $h = 100$ nm, as well as the values of $\alpha$ for 50-SB1, 50-SB2, and 50-SB3 are determined to be 71°, 70°, and 61° when $h = 50$ nm, respectively. In addition, those values for 25-SB1 and 25-SB2 are 155° and 149° when $h = 25$ nm, as well as 158°, 154°, and 144° when $h = 10$ nm, respectively. In addition, the calculated shear strains of the Cu/CrCoNi composites with $h = 100$, 50, 25, and 10 nm are plotted in Fig. 12a and b, which clearly show that the sample with $h = 100$ nm possesses the lowest shear strain, whereas the shear strain is significantly increased in the smaller-layer-thickness samples with $h = 50$, 25, and 10 nm. For example, taking the maximum shear strain ($\gamma_{max}$) of the samples as the measurement index, the $\gamma_{max}$ values of the samples with $h = 100$, 50, 25, and 10 nm are calculated to be 0.48, 1.48, 1.54, and 1.57, respectively. The $\gamma_{max}$ value is decreased by 69% when $h$ increases from 10 to 100 nm, demonstrating that the severest strain localization occurs in the sample with $h = 10$ nm (Fig. 12c). The calculated values of maximum strain localization parameter ($\xi_{p,max}$) of the samples with $h = 100$, 50, 25, and 10 nm are 1.50, 4.81, 6.11, and 10.74, respectively, indicating a reduction of shear instability with almost one order of magnitude with the increase of $h$. In addition, it is obvious that $\xi_{p,max}$ shows a monotonically increase when $h$ decreases from 100 to 10 nm, which is well consistent with the $\gamma_{max} - h$ relation. The above results clearly demonstrate that the shear instability of the Cu/CrCoNi composites is strongly size-dependent.

The prediction of the shear banding direction has been given in the following by considering the orientation of the dislocation gliding plane and the maximum shear stress direction as well as their relationships in the developed theoretical model (Fig. 13). Accordingly, the shear band direction can be determined by the coupling effect of the maximum shear stress direction (i.e., $\omega = 45°$, Fig. 13b–d) and the orientation of the activated slip planes that are rotated towards the maximum shear stress plane following the kinking of the interfaces during deformation, as illustrated in Fig. 13. It is reasonable to assume that the shear banding occurs in a direction that coincides with or is close to the orientation of the dislocation gliding plane. However, the orientation of the activated

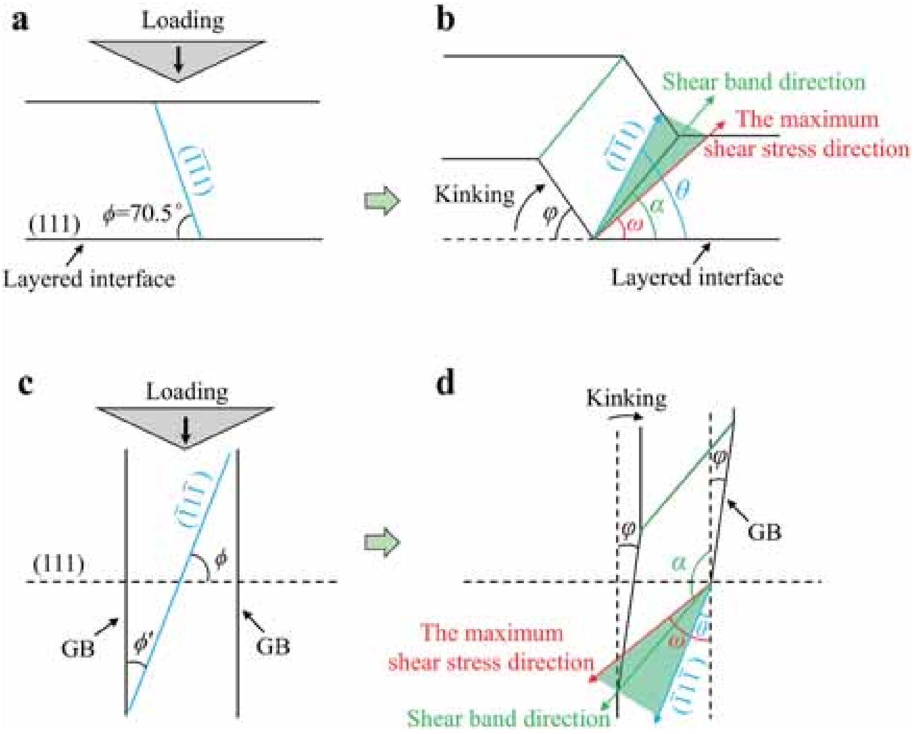

**Fig. 13.** Schematic illustration of the shear banding direction in the samples with (a, b) $h > 25$ nm and (c, d) $h \leq 25$ nm. (a, c) The activated slip planes during micro-indentations. (b, d) The range of the shear banding direction. $\phi = 70.5^\circ$ denotes the angle between the orientation of the activated slip plane and the horizontal layered interface, while $\phi' = \pi/2 - \phi$ is the angle between the slip plane $(\bar{1}1\bar{1})$ and the vertical GB, i.e., 19.5°. $\omega = 45^\circ$ indicates the maximum shear stress direction, $\theta$ represents the angle between the slip plane after rotation and the original layered interfaces or vertical GBs, $\alpha$ designates the tilting angle of the shear band, and $\varphi$ denotes the kinking angle of the horizontal layered interface or the vertical GB.

slip plane generally deviates from the maximum shear stress direction (Fig. 13a–c). Therefore, the interfaces (horizontal layered interfaces or GBs) must kink to rotate the activated slip plane towards the maximum shear stress direction. Finally, the shear banding occurs if the orientation of the rotated slip plane coincides with or is close to the maximum shear stress direction. As a result, the shear banding direction lies between the orientation of the rotated slip plane and the maximum shear stress direction (see the green shaded area in Fig. 13b–d).

For the case of shear banding induced by the kinking of the horizontal layered interface (i.e., as $h > 25$ nm), the original plane of the constituent layers lies normal to the loading direction. In this condition, the $(\bar{1}11)$ slip planes (70.5° to the horizontal layered interface) are activated in priority, whereas the (111) slip planes parallel to the interface are not favored (Fig. 13a) because the Schmid factor of the former (0.27) is larger than that of the latter (zero). With further loading, the geometric stress concentrations of the Vickers indenter tip exert a nonuniaxial stress state, causing a rotation of the layers, thereby bringing the $(\bar{1}11)$ slip plane towards the maximum shear stress plane (45° to the layered interface, i.e., $\omega$ in Fig. 13b), and eventually leading to shear banding. The angle between the $(\bar{1}11)$ slip plane after rotation and the original layered interface is $\theta$. Then, the tilting angle of the SB ($\alpha$) should be located between the maximum shear stress plane and $\theta$, as indicated by the green shaded area in Fig. 13b. In this case, we can obtain $45^\circ < \alpha < \theta < 90^\circ$.

For the case of shear banding induced by the kinking of the vertically aligned grain boundary (GB) (i.e., as $h \leq 25$ nm), the slip events may be concentrated in $(\bar{1}1\bar{1})$ slip plane (70.5° to the horizontal layered interface, i.e., $\phi$ as indicated in Fig. 13c) with Schmid factor of 0.27 in [110] slip direction. This is because the shear banding at $h \leq 25$ nm is induced by a small kinking angle $\varphi$ (21°–25°, see Table 2) of the vertical GBs. This deformation indicates that the activated $(\bar{1}1\bar{1})$ slip plane can approach the maximum shear stress plane only by a small angle rotation, thus leading to shear banding, as schematized in Fig. 13d. In this case, the SB direction is located between the maximum shear stress direction and the $(\bar{1}1\bar{1})$ slip plane, as denoted by the green shaded area in Fig. 13d. Then, the tilting angle of the SB is in the range of $\pi-\omega$ to $\pi-\theta$, i.e., $\pi - \omega < \alpha < \pi - \theta$. Here $\theta$ should be larger than $\phi'$ (19.5°) due to the kinking of the vertical GBs towards the clockwise direction. Thus, we have $135^\circ < \alpha < 160.5^\circ$.

Based on the above analysis, it can be concluded that the SB forms as the activated slip planes rotate to coincide nearly with the maximum shear stress plane. As a consequence, the measured tilting angles of the SBs in experiments are in good agreement with the theoretical model-predicted one, as summarized in Table 2. It should be pointed out that the $\theta$ is hard to determine due to the complex slip events in the polycrystalline material, especially under the complex stress states. Nevertheless, the theoretical model gives a quantitative prediction for the range of the SB direction, that is $45^\circ < \alpha < 90^\circ$ for the shear banding

**Table 2**
The measured tilting angle ($\alpha$) of the shear band (SB) and the maximum kinking angle ($\varphi_{\max}$) of the horizontal layered interface or the vertical aligned grain boundary for Cu/CrCoNi composites.

| SB | $\alpha$ (°) | $\varphi_{\max}$ (°) | $45^\circ < \alpha < 90^\circ$? | $135^\circ < \alpha < 160.5^\circ$? |
|---|---|---|---|---|
| | Experimental | Experimental | Theoretical | Theoretical |
| 100-SB1 | 59 | 46 | Yes | / |
| 50-SB1 | 71 | 73 | Yes | / |
| 50-SB2 | 70 | 79 | Yes | / |
| 50-SB3 | 61 | 76 | Yes | / |
| 25-SB1 | 155 | 23 | / | Yes |
| 10-SB1 | 149 | 25 | / | Yes |
| 10-SB2 | 158 | 21 | / | Yes |
| 10-SB3 | 154 | 24 | / | Yes |

induced by the kinking of the horizontal layered interface, and $135^\circ < \alpha < 160.5^\circ$ for the shear banding induced by the kinking of the vertically aligned GB.

In conclusion, the theoretical model gives a unified mechanics expression (Eq. (2)) for calculating the shear strain ($\gamma$) for the two shear banding modes mediated by the kinking of the horizontal layered interfaces or the vertically aligned GBs. In addition, the range of the shear banding direction can also be predicted based on the relationship between the orientation of the dislocation gliding plane and the maximum shear stress direction. The proposed theoretical model provides a fundamental tool, which is otherwise absent in all existing studies, to quantify the degree of the shear banding either dominated by the horizontal layered interfaces or the vertical GBs. The developed model can be used to evaluate the layer thickness-dependent shear instability, including the magnitude of shear banding-induced strain localization and the shear banding direction, for medium entropy alloy based nanolayered metallic composites.

## 4. Discussion

### *4.1. The strengthening mechanism of Cu/CrCoNi composites*

As mentioned previously, the hardness of the Cu/CrCoNi composites monotonically increases with the decrease of $h$ (Fig. 6b). In this section, the underlying strengthening mechanism of the Cu/CrCoNi composites will be discussed. Fig. 14 provides the yield strength ($\sigma$) as a function of the layer thickness or grain size for the Cu/CrCoNi composites, where $\sigma$ is estimated via the Tabor relation $\sigma = H/2.7$ (Liu et al., 2011; Mompiou et al., 2012). The findings in the previous sections have demonstrated that the shear instabilities of all samples with different layer thicknesses are all induced by the cooperative kinking of interfaces, namely the layered interfaces in the samples with large layer thicknesses or the aligned GBs in those with small layer thicknesses.

Therefore, the refined CLS model proposed by Misra et al. (2005a) that incorporates the effect of dislocation core spreading along the interface, interface stress, and dislocation-dislocation interactions (Fan et al., 2017; Zhao et al., 2019) can be used to estimate the yield strength of the Cu/CrCoNi composites with $h = 2$–$100$ nm, i.e.,

$$\sigma_{\mathrm{CLS}} = \frac{M\mu b \sin\theta}{8\pi s}\left(\frac{4-\nu}{1-\nu}\right)\ln\left(\frac{As}{b\sin\theta}\right) - \frac{F}{s} + \frac{\mu\varepsilon}{1-\nu} \tag{6}$$

where $s$ represents the distance (i.e., interface spacing) between two neighboring layered interfaces or GBs, i.e., $h$ or $d$. M, $\mu$, $b$, $\theta$, and $\nu$ represent the Taylor factor, the shear modulus, the magnitude of Burgers vector of a full dislocation, the angle between the interface and the slip plane, and the Poisson ratio, respectively. And $A$ is the core cut-off parameter in the range from 0 to 1 (Misra et al., 2005a), $F$ is the characteristic interface stress, typically 2–3 J $\mathrm{m}^{-2}$ for crystalline/crystalline interfaces (Misra et al., 2005a), and $\varepsilon$ is the in-plane plastic strain in the range of 1%–2%. By using the following parameters, i.e., $\mathrm{M} = 3.06$, $\mu_{\mathrm{Cu}} = 48$ GPa (Zhao et al., 2019), $b_{\mathrm{f,Cu}} = 0.2556$ nm (Zhao et al., 2018), $\theta = 70.5^{\mathrm{o}}$, $\nu_{\mathrm{Cu}} = 0.343$ (Zhao et al., 2018), $A = 1$, $F = 3$ J $\mathrm{m}^{-2}$, and $\varepsilon = 1.9\%$, we obtain the relation between the CLS stress and layer thickness/grain size of the Cu/CrCoNi composites as shown in Fig. 14. It can be found that the CLS model shows a good prediction of the strength of the Cu/CrCoNi composites.

It is believed that it is the GB, instead of the layered interface, that contributes to the continuous strengthening of Cu/CrCoNi composites with $h \leq 25$ nm for the following reasons. It is wildly accepted that the dislocation across the interface occurs at the layer thickness of 2–5 nm (Misra et al., 2005a) in deposited metallic nanolayered composites, which determines the peak strength of the composites (Su et al., 2021). Thus, one may expect that parts of dislocations can transmit across the layered interfaces in the present 5 nm and 2 nm Cu/CrCoNi samples since there exist parallel slip directions in the Cu and CrCoNi layers as demonstrated by the TEM analysis (Fig. 3j and l). Then, the strength of the composite will reach a maximum and even decrease in the layer thickness of 5 and 2 nm. However, it can be seen that the Cu/CrCoNi composites show a continuous strengthening even the layer thickness is reduced down to 2 nm (see Fig. 14). Therefore, this finding indicates that the continuous strengthening below 5 nm in the composite might result from the bowing of dislocations between the vertically aligned GBs. In this case, the CLS stress is significantly reduced because the grain size is much larger than the layer thickness (e.g., $d = 27$ nm for the 2 nm sample), see the CLS model predictions for $h \leq 25$ nm (the empty circles in the red solid line). As a result, the transmission of dislocations across the layered interfaces will not occur. Instead, the bowing of the dislocations between the aligned GBs is stimulated to contribute to the continuous strengthening of the composite.

Moreover, except for the samples with $h = 5$ and 2 nm, the yield strength of the composites is basically consistent with the predicted values of the CLS model. The reason why the yield strength of the Cu/CrCoNi composites with $h = 5$ and 2 nm is slightly higher than that predicted by the CLS model is that abundant nanotwins can make significant strengthening in nanostructured metallic materials, as demonstrated by extensive experiments, atomic simulations, and theoretical analysis (Li et al., 2010a, 2020b; Lu et al., 2009). Previous atomic simulations (Li et al., 2010a) demonstrated that the strengthening-to-softening transition will not occur if the twin–boundary spacing is larger than 1.2 nm for nanotwinned Cu with $d = 10$ nm. In this paper, the thickness of nanotwins is around 2 nm, larger than the above-mentioned critical size, and the layer thicknesses of the Cu and CrCoNi layers are refined to 5 and 2 nm. Therefore, continuous strengthening was observed in the Cu/CrCoNi composites with $h = 5$ and 2 nm.

In addition, the reported data in conventional Cu/Ni (Liu et al., 2011), Cu/Co (Liu et al., 2013), and Cu/Cr (Misra et al., 1998) composites are included in Fig. 14 for comparison. The results show that the yield strength of the Cu/CrCoNi composites is significantly higher than that of *fcc*/*fcc* Cu/Ni and Cu/Co composites, and its value at small $h$ ($h \leq$

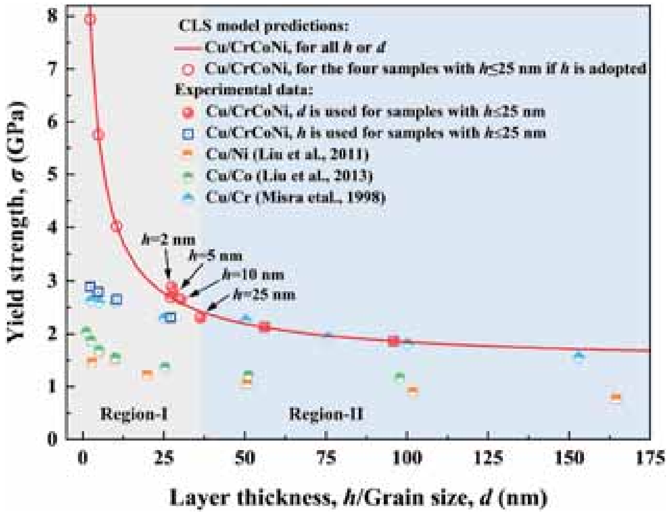

**Fig. 14.** The dependence of yield strength on the layer thickness/grain size for the Cu/CrCoNi composites, and the comparison of yield strength between the Cu/CrCoNi composites and the reported bi-metal Cu/Ni (Liu et al., 2011), Cu/Co (Liu et al., 2013), and Cu/Cr (Misra et al., 1998) composites. The red solid curve is obtained based on the CLS model. For the plotting of the experimental data of Cu/CrCoNi composites, grain size d was adopted for the samples with $h \leq 25$ nm (region-I), otherwise the actual layer thickness h was used when $h > 25$ nm (region-II). The experimental data adopted for comparison were all plotted by using layer thickness. (For interpretation of the references to colour in this figure legend, the reader is referred to the Web version of this article.)

10 nm) is even higher than that of *fcc*/body-centered cubic (*bcc*) Cu/Cr composites. This result suggests that compared to bi-metal Cu/X (X = Cr, Co, Ni) composites, the Cu/CrCoNi composites have great advantages in practical usage due to their ultrahigh strength.

### *4.2. The shear banding mechanisms of Cu/CrCoNi composites*

According to the above-mentioned residual indentation morphologies and the corresponding quantitative analyses about the degree of shear instability, it is clear that all Cu/CrCoNi composites exhibit the same shear instability mode in the form of kinking-like shear banding. However, the cooperative kinking-like shear banding is mediated by totally different interfaces, namely the aligned GBs in the samples with $h \leq 25$ nm and the layered interfaces in those with $h > 25$ nm. Combined with the strengthening mechanism, two underlying layer-thickness-dependent deformation mechanisms of the Cu/CrCoNi composites with $h$ varying from 2 to 100 nm will be discussed in this section.

Next, we consider the influence of the dislocation mechanism on the SB formation in the Cu/CrCoNi composites. For the Cu/CrCoNi composite with a relatively small layer thickness ($h \leq 25$ nm) (Fig. 15, Region-I), the dislocation is believed to be bowing between the adjacent vertically aligned GBs (instead of the horizontal layered interfaces) due to $d > h$ because a lower stress is required to propagate the gliding dislocation loop in the former than in the latter (as seen in Fig. 5, where $d$ represents the grain size) according to the CLS model (Misra et al., 2005a), i.e., Eq. (6), which is inversely proportional to layer thickness or grain size. The dislocation seems to be moving almost parallel to the layered interface because the interface spacing made by the constituent layers is much smaller than that by the GBs (i.e., small $h$ versus large $d$). Actually, the dislocation is moving in a slip plane (the blue one) with a specific angle to the horizontal layered interface (e.g., typical 70.5° for {111} planes to the horizontal interface plane) that is bound by the vertical GBs (the yellow planes in Fig. 15).

However, for the case of $h > 25$ nm, the dislocation glides by Orowan bowing in its slip plane that is bound by the horizontal layered interfaces (instead of the vertical GBs, see Region-II in Fig. 15), which is similar to the observed confined layer slip in the Cu/Nb nanolayered composite by in situ nano-indentation experiments in TEM (Li et al., 2012b). In this case, the dislocation is bowing between the horizontal layered interfaces (the green planes in Fig. 15), instead of the vertical GBs, due to the smaller stress required to propagate the gliding dislocation loop in the former than that in the latter since $h > d$ according to Eq. (6). Physically, the deformation modes for the two size regions are identical, that is, the dislocation is bowing out between interfaces. The only difference lies in the specific type of interfaces, i.e., the horizontal layered interfaces or the vertical aligned GBs.

The corresponding dislocation activities of the above two deformation modes are elucidated in the following. First, the dislocation is nucleated from the layered interface in the Cu/CrCoNi composite due to the atomically intense interface distortions, i.e., misfit dislocations. This physic mechanism has been validated by in situ nano-indentation in TEM (Li et al., 2012b) and atomic simulations (Zhang et al., 2011; Cheng and Trelewicz, 2016). Though GB can act as the dislocation source, there are only few dislocations that nucleate from the GB in the nanolayered composite as demonstrated by the atomic simulations (Cheng and Trelewicz, 2016). Therefore, in the case of small layer thickness ($h < 25$ nm), a dislocation (indicated by the number '1' in Region-I of Fig. 15) first nucleates from the layered interface and propagates within the slip

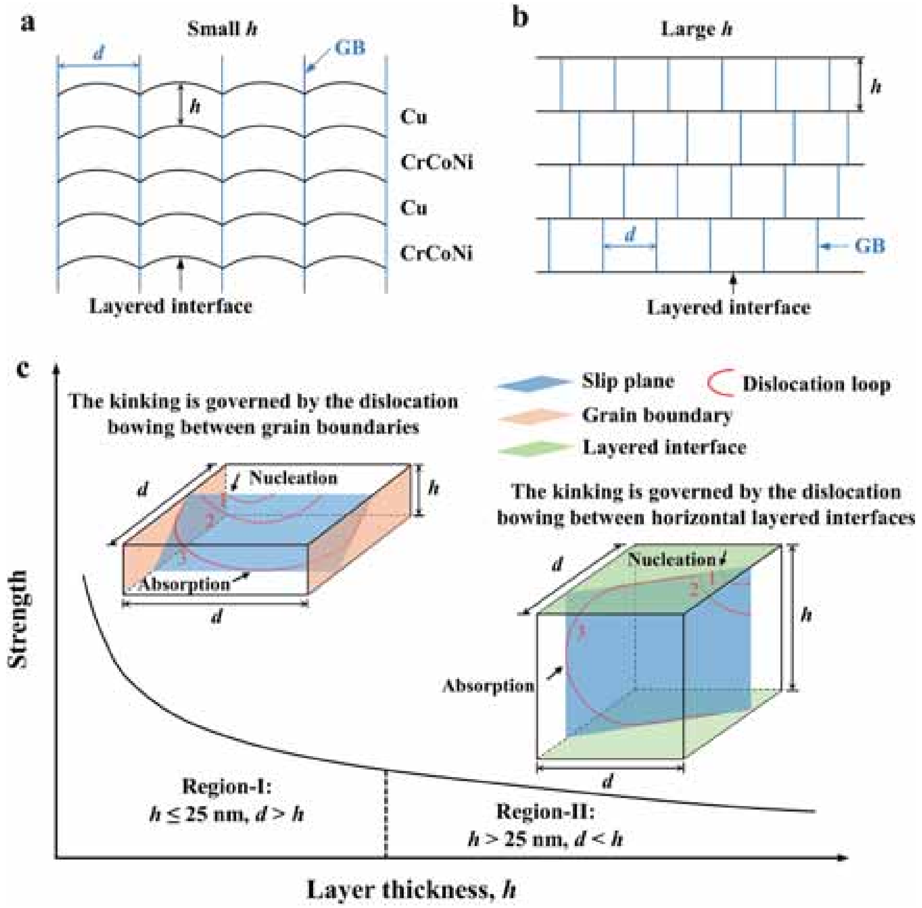

**Fig. 15.** Schematic diagrams of the microstructures of the Cu/CrCoNi composites with (a) small and (b) large $h$. (c) Schematic illustration of the underlying mechanism of the size-dependent shear instability of the Cu/CrCoNi composites as a function of the layer thickness.

plane to form a dislocation loop (number ‘2’). With strain processing, the bowing dislocation will be bound by the GB and slip in the slip plane until it reaches the neighboring layered interface. Then, the gliding dislocation (number ‘3’) would get blocked at the layered interface due to the formed stacking faults near the layered interface (as seen in Fig. 3j and l), which is a very strong barrier to slip since the transmission requires the creation of a jog line or stair-rod dipole (Hoagland et al., 2002). With further loading, the dislocation would penetrate the stacking fault planes (Li et al., 2023), and then the layered interface can shear in response to the stress field of the glide dislocation that approaches the layered interface, leading to the absorption of the gliding dislocation in the layered interface (Wang et al., 2011). Subsequently, the next plasticity events will occur (stochastically) at other locations along the GB.

For $h > 25$ nm, the dislocation also nucleates from the layered interface and propagates within the slip plane, similar to the case of small layer thickness. The difference is that the dislocation is bowing between the horizontal layered interfaces, instead of the vertical GBs, due to the larger interface spacing in the former than that in the latter. Thus, the gliding dislocation moves within the slip plane until it is absorbed in a columnar GB (Misra et al., 2004; Li et al., 2012b), as schematized in Region-II of Fig. 15. It is admitted that there is a lack of direct experimental observation for the above dislocation activities that could be obtained by in-situ nano-indentation tests in TEM, as conducted by Li et al. (2012b) for Cu/Nb nanolayered composite. However, the investigation on the present material by this in-situ test is out of the scope of this study.

The above conclusion on the dislocation mechanism was made based on the following experimental and theoretical evidences: (i) the shear banding of the composite in all the samples with $h \leq 25$ nm is governed by the kinking of the vertically aligned GBs (Fig. 9), which is in a clear contrast to the kinking of the horizontally arranged layered interfaces in those with $h > 25$ nm (Fig. 8). (ii) The CLS model can be used to well reproduce the size-dependent strength of the composites with $h \leq 25$ nm only if the grain size $d$ (rather than the layer thickness $h$) was adopted to be the size parameter in Eq. (6) (Fig. 14). In contrast, the model predictions are much higher than the experimental measurements if the layer thickness was employed in the CLS model (see the red circles versus the blue squares in Fig. 14) because $h$ is much smaller than $d$ (see Fig. 5).

Besides, it is well known that the dislocation transmission across the interface is associated with many factors, such as the orientation relationship, elastic moduli mismatch and lattice parameter mismatch between constituent phases (Hunter et al., 2018). Particularly, the orientation relationship plays a key role in the dislocation transmission, which even alters the shear banding mechanism. It can be seen that SFs on basal planes and twins are mostly observed near the interfaces (Fig. 3d–f, h, j, l). Therefore, the dislocation reaching the interface will be extremely blocked due to the existence of high-density SFs near the interface and hetero-twin interface with mirror symmetry orientation, i.e., the slip directions are not well aligned. Consequently, these blocked dislocations by the interface/GB can cause the interface/GB to slide, which in turn attracts and traps the impinging dislocation, and once absorbed causes its core to spread within the interface instead of crossing the interface (Wang et al., 2011). The interface/GB sliding produced by this dislocation mechanism combined with the titling of interface/GB induced by the stress concentration (generated by the Vicker indenter) leads to the shear banding in the Cu/CrCoNi composites. In contrast, the case of the dislocation transmission across the interface usually induced the crystallographic banding as observed in Cu/Nb composite with facet interface (Zheng et al., 2014).

Furthermore, the transition of the deformation modes from the vertically aligned GBs-accommodated kinking to the horizontal layered interfaces-mediated one in the Cu/CrCoNi composites results from the competition of these two modes (Fig. 15). When $h \leq 25$ nm, the grain sizes are much larger than the layer thicknesses (Fig. 5), leading to a much smaller CLS stress based on the GBs-mediated cooperative kinking (here $d$ is used in Eq. (6)) than that based on the layer interfaces-dominated one (here $h$ is used in Eq. (6)). Furthermore, in such scale, the GBs are vertically aligned, whereas the layered interfaces are wavy (Fig. 2g–r and Fig. 15a). Therefore, the shear banding in the composites with $h \leq 25$ nm is governed by the cooperative kinking of the vertically aligned GBs. However, when the layer thickness is sufficiently large ($h >$ 25 nm), the grain sizes are smaller than the layer thicknesses (Fig. 5). And more importantly, the layered interfaces are successive, which is not the case in the GBs in the vertical direction (Fig. 2a–f and Fig. 15b). Thus, the shear banding is dominated by the cooperative kinking of the layered interfaces, which requires much smaller CLS stress than the cooperative kinking of the GBs.

In addition to dislocation motion, abundant nanotwins in the CrCoNi layers also participate in deformation. For instance, in similar CrCoFeNi HEA materials with low SFE, it was observed through experiments and molecular dynamics simulations that the dominated deformation mechanism of the <100>-orientation is deformation twinning (Cao et al., 2023; Zhang et al., 2022). The nanotwin nucleation resulted from the slip of the pre-existing partial dislocations from an internal source. Also, the in situ tension shows that the <110>-oriented CrCoFeNi nanopillar possesses a super high room-temperature uniform elongation (up to 110%), owing to the spatial and synergetic coordination of deformation twinning and dislocation slip (Zhang et al., 2023). As a result, it can be speculated that the deformation of the CrCoNi layers in the Cu/CrCoNi composites is dominated by dislocation slip, deformation twinning, and twin-dislocation interactions (Liang et al., 2021; Liu et al., 2022; Zeng and Li, 2021).

## 5. Concluding remarks

In this work, the strengthening and shear instability of the Cu/CrCoNi composites with various layer thicknesses ($h = 2$–100 nm) have been systematically investigated by both nano/microindentation experiments. A theoretical model has been developed to quantify the shear instability. The main findings are summarized as follows.

(1) The hardness of the Cu/CrCoNi composites increases monotonically with the decrease of $h$, manifesting the trend of “smaller is stronger”. The hardness of the samples reaches the maximum value of $7.8 \pm 0.2$ GPa at $h = 2$ nm, which is much higher than the predicted value (5.3 GPa) based on the ROM. In addition, the strengthening effects of all samples can be well described by the refined CLS model.

(2) As indicated by the microindentation tests and the theoretical analysis, the deformation of all Cu/CrCoNi composites is dominated by cooperative kinking-like shear banding. However, the shear banding of the samples with $h > 25$ nm is mediated by the horizontal layered interfaces that collaborate to kink together, whereas that of the others is mediated by the vertically aligned GBs of all columnar grains. Furthermore, the degree of shear instability increases with the decrease of the layer thickness.

Different from the popular belief, it is found that the shear deformation is mediated by the vertically aligned GBs rather than the horizontal layered interfaces due to the occurrence of the columnar crystal when $h \leq 25$ nm. These findings give valuable insights into explaining the behavior of shear deformation for the nanolayered composites that contain M/HEAs as the constituent phases. In addition, the developed theoretical model provides a convenient and effective route to evaluate the plasticity of nanolayered metallic composites by several simple micro-indentations, in which the time consuming and costly micropillar-compression tests and the following complicated TEM characterization of the deformed pillars could be avoided.

## CRediT authorship contribution statement

**Feng Qin:** Writing – review & editing, Visualization, Investigation, Formal analysis. **Kaiqing Dai:** Formal analysis, Investigation, Visualization. **Junhua Hou:** Investigation. **Wenjun Lu:** Writing – review & editing. **Shaohua Chen:** Writing – review & editing. **Jianjun Li:** Writing – review & editing, Resources, Project administration, Funding acquisition, Conceptualization, Methodology.

## Declaration of competing interest

The authors declare that they have no known competing financial interests or personal relationships that could have appeared to influence the work reported in this paper.

## Data availability

Data will be made available on request.

## Acknowledgements

This work was financially supported by the National Natural Science Foundation of China (NSFC) (Grant No. 12272413), the Department of Science and Technology of Hunan Province, China (Grant No. 2021RC3022), and the Project of State Key Laboratory of Precision Manufacturing for Extreme Service Performance, Central South University (Grant No. ZZYJKT2024-11).

## References

Bajpai, S., MacDonald, B.E., Rupert, T.J., Hahn, H., Lavernia, E.J., Apelian, D., 2022. Recent progress in the CoCrNi alloy system. Materialia 24, 101476.

Beyerlein, I.J., Demkowicz, M.J., Misra, A., Uberuaga, B.P., 2015. Defect-interface interactions. Prog. Mater. Sci. 74, 125–210.

Bhattacharyya, D., Mara, N.A., Dickerson, P., Hoagland, R.G., Misra, A., 2009. Transmission electron microscopy study of the deformation behavior of Cu/Nb and Cu/Ni nanoscale multilayers during nanoindentation. J. Mater. Res. 24, 1291–1302.

Cantor, B., Chang, I.T.H., Knight, P., Vincent, A.J.B., 2004. Microstructural development in equiatomic multicomponent alloys. Mater. Sci. Eng., A 375, 213–218.

Cao, T., Zhang, Q., Wang, L., Wang, L., Xiao, Y., Yao, J., Liu, H., Ren, Y., Liang, J., Xue, Y., Li, X., 2023. Dynamic deformation behaviors and mechanisms of CoCrFeNi high-entropy alloys. Acta Mater. 260, 119343.

Cao, Z.H., Cai, Y.P., Sun, C., Ma, Y.J., Wei, M.Z., Li, Q., Lu, H.M., Wang, H., Zhang, X., Meng, X.K., 2019a. Tailoring strength and plasticity of Ag/Nb nanolaminates via intrinsic microstructure and extrinsic dimension. Int. J. Plast. 113, 145–157.

Cao, Z.H., Ma, Y.J., Cai, Y.P., Wang, G.J., Meng, X.K., 2019b. High strength dual-phase high entropy alloys with a tunable nanolayer thickness. Scripta Mater. 173, 149–153.

Chen, H., Chen, K.-H., Xu, Y.-c., Pan, C.-x., Yi, J.-y., Zhu, C.-j., 2018. Microstructure, mechanical properties, and milling performance of arc-PVD AlTiN-Cu and AlTiN/AlTiN-Cu coatings. J. Cent. S. Univ. 25, 506–515.

Chen, Y., Liu, Y., Sun, C., Yu, K.Y., Song, M., Wang, H., Zhang, X., 2012. Microstructure and strengthening mechanisms in Cu/Fe multilayers. Acta Mater. 60, 6312–6321.

Chen, Y., Liu, Y., Fu, E.G., Sun, C., Yu, K.Y., Song, M., Li, J., Wang, Y.Q., Wang, H., Zhang, X., 2015. Unusual size-dependent strengthening mechanisms in helium ion-irradiated immiscible coherent Cu/Co nanolayers. Acta Mater. 84, 393–404.

Chen, Y., Li, N., Hoagland, R.G., Liu, X.Y., Baldwin, J.K., Beyerlein, I.J., Cheng, J.Y., Mara, N.A., 2020. Effects of three-dimensional Cu/Nb interfaces on strengthening and shear banding in nanoscale metallic multilayers. Acta Mater. 199, 593–601.

Cheng, B., Trelewicz, J.R., 2016. Mechanistic coupling of dislocation and shear transformation zone plasticity in crystalline-amorphous nanolaminates. Acta Mater. 117, 293–305.

Cui, Y., Derby, B., Li, N., Mara, N.A., Misra, A., 2018. Suppression of shear banding in high-strength Cu/Mo nanocomposites with hierarchical bicontinuous intertwined structures. Materials Research Letters 6, 184–190.

Ding, Q., Fu, X., Chen, D., Bei, H., Gludovatz, B., Li, J., Zhang, Z., George, E.P., Yu, Q., Zhu, T., Ritchie, R.O., 2019. Real-time nanoscale observation of deformation mechanisms in CrCoNi-based medium- to high-entropy alloys at cryogenic temperatures. Mater. Today 25, 21–27.

Dong, S.J., Chen, T.J., Huang, S.X., Li, N., Zhou, C.Z., 2020. Thickness-dependent shear localization in Cu/Nb metallic nanolayered composites. Scripta Mater. 187, 323–328.

Dong, S.J., Liu, X.Y., Chen, Y.X., Zhou, C.Z., 2023. Atomistic analysis of plastic deformation and shear band formation in FCC/FCC metallic nanolayered composites. J. Mater. Res. 38, 1386–1395.

Fan, Z., Liu, Y., Xue, S., Rahimi, R.M., Bahr, D.F., Wang, H., Zhang, X., 2017. Layer thickness dependent strain rate sensitivity of Cu/amorphous CuNb multilayer. Appl. Phys. Lett. 110, 161905.

Fu, E.G., Li, N., Misra, A., Hoagland, R.G., Wang, H., Zhang, X., 2008. Mechanical properties of sputtered Cu/V and Al/Nb multilayer films. Mater. Sci. Eng., A 493, 283–287.

Gludovatz, B., Hohenwarter, A., Thurston, K.V.S., Bei, H., Wu, Z., George, E.P., Ritchie, R.O., 2016. Exceptional damage-tolerance of a medium-entropy alloy CrCoNi at cryogenic temperatures. Nat. Commun. 7, 10602.

Gu, C., Wang, F., Huang, P., Xu, K.W., Lu, T.J., 2016. Structure-dependent size effects in CuTa/Cu nanolaminates. Mater. Sci. Eng., A 658, 381–388.

Hoagland, R.G., Mitchell, T.E., Hirth, J.P., Kung, H., 2002. On the strengthening effects of interfaces in multilayer fcc metallic composites. Philos. Mag. A 82, 643–664.

Holmberg, K., Matthews, A., Ronkainen, H., 1998. Coatings tribology—contact mechanisms and surface design. Tribol. Int. 31, 107–120.

Huang, G.Y., Zhang, X.Q., Xie, Z.C., Jian, W.R., Zhang, R., Yao, X.H., 2023. Effects of lattice distortion and chemical short-range order on creep behavior of medium-entropy alloy CoCrNi. Mech. Mater. 177, 104549.

Huang, L., Chen, Z.Q., Huang, P., Meng, X.K., Wang, F., 2020. Irradiation-induced homogeneous plasticity in amorphous/amorphous nanolaminates. J. Mater. Sci. Technol. 57, 70–77.

Hunter, A., Leu, B., Beyerlein, I.J., 2018. A review of slip transfer: applications of mesoscale techniques. J. Mater. Sci. 53 (8), 5584–5603.

Jiang, L., Powers, M., Cui, Y., Derby, B.K., Misra, A., 2021. Microstructure and mechanical properties of nanoscale Cu/(Ta50Nb25Mo25) multilayers. Mater. Sci. Eng., A 799, 140200.

Kang, K., Wang, J., Zheng, S.J., Beyerlein, I.J., 2012. Minimum energy structures of faceted, incoherent interfaces. J. Appl. Phys. 112, 073501.

Khallaf, A.H., Bhlol, M., Dawood, O.M., Elkady, O.A., 2022. Wear resistance, hardness, and microstructure of carbide dispersion strengthened high-entropy alloys. J. Cent. S. Univ. 29, 3529–3543.

Laplanche, G., Bonneville, J., Varvenne, C., Curtin, W.A., George, E.P., 2018. Thermal activation parameters of plastic flow reveal deformation mechanisms in the CrMnFeCoNi high-entropy alloy. Acta Mater. 143, 257–264.

Lei, S., Zhang, J.Y., Niu, J.J., Liu, G., Zhang, X., Sun, J., 2012. Intrinsic size-controlled strain hardening behavior of nanolayered Cu/Zr micropillars. Scripta Mater. 66, 706–709.

Lei, Z., Liu, X., Wu, Y., Wang, H., Jiang, S., Wang, S., Hui, X., Wu, Y., Gault, B., Kontis, P., Raabe, D., Gu, L., Zhang, Q., Chen, H., Wang, H., Liu, J., An, K., Zeng, Q., Nieh, T.-G., Lu, Z., 2018. Enhanced strength and ductility in a high-entropy alloy via ordered oxygen complexes. Nature 563, 546–550.

Li, J., Wang, Y., Yan, D., Li, J., 2023. Effects of nanotwins and stacking faults on the mechanical properties of CrCoNi medium-entropy alloys. J. Mater. Res. Technol. 27, 3447–3458.

Li, X., Lu, L., Li, J., Zhang, X., Gao, H., 2020b. Mechanical properties and deformation mechanisms of gradient nanostructured metals and alloys. Nat. Rev. Mater. 5, 706–723.

Li, J.J., Lu, W.J., Zhang, S.Y., Raabe, D., 2017. Large strain synergetic material deformation enabled by hybrid nanolayer architectures. Sci. Rep. 7.

Li, J.J., Lu, W.J., Gibson, J., Zhang, S.Y., Chen, T.Y., Korte-Kerzel, S., Raabe, D., 2018b. Eliminating deformation incompatibility in composites by gradient nanolayer architectures. Sci. Rep. 8, 16216.

Li, Z., Pradeep, K.G., Deng, Y., Raabe, D., Tasan, C.C., 2016b. Metastable high-entropy dual-phase alloys overcome the strength–ductility trade-off. Nature 534, 227–230.

Li, J.J., Qin, F., Yan, D.S., Lu, W.J., Yao, J.H., 2022. Shear instability in heterogeneous nanolayered Cu/Zr composites. J. Mater. Sci. Technol. 105, 81–91.

Li, N., Nastasi, M., Misra, A., 2012a. Defect structures and hardening mechanisms in high dose helium ion implanted Cu and Cu/Nb multilayer thin films. Int. J. Plast. 32–33, 1–16.

Li, N., Wang, J., Misra, A., Huang, J.Y., 2012b. Direct observations of confined layer slip in Cu/Nb multilayers. Microsc. Microanal. 18, 1155–1162.

Li, J.J., Lu, W.J., Gibson, J., Zhang, S.Y., Korte-Kerzel, S., Raabe, D., 2020a. Compatible deformation and extra strengthening by heterogeneous nanolayer composites. Scripta Mater. 179, 30–35.

Li, X., Wei, Y., Lu, L., Lu, K., Gao, H., 2010a. Dislocation nucleation governed softening and maximum strength in nano-twinned metals. Nature 464, 877–880.

Li, Y.P., Zhu, X.F., Tan, J., Wu, B., Wang, W., Zhang, G.P., 2009a. Comparative investigation of strength and plastic instability in Cu/Au and Cu/Cr multilayers by indentation. J. Mater. Res. 24, 728–735.

Li, Y.P., Zhu, X.F., Tan, J., Wu, B., Zhang, G.P., 2009b. Two different types of shear-deformation behaviour in Au–Cu multilayers. Phil. Mag. Lett. 89, 66–74.

Li, D., Zhu, Z.W., Wang, A.M., Fu, H.M., Li, H., Zhang, H.W., Zhang, H.F., 2018a. New ductile laminate structure of Ti-alloy/Ti-based metallic glass composite with high specific strength. J. Mater. Sci. Technol. 34, 708–712.

Li, J., Chen, Y., Xue, S., Wang, H., Zhang, X., 2016a. Comparison of size dependent strengthening mechanisms in Ag/Fe and Ag/Ni multilayers. Acta Mater. 114, 154–163.

Li, Z., He, H., Cao, H., Sun, S., Diao, W., Gao, D., Lu, P., Zhang, S., Guo, Z., Li, M., Liu, R., Ren, D., Liu, C., Zhang, Y., Yang, Z., Jiang, J., Zhang, G., 2019. Atomic Co/Ni dual sites and Co/Ni alloy nanoparticles in N-doped porous Janus-like carbon frameworks for bifunctional oxygen electrocatalysis. Appl. Catal. B Environ. 240, 112–121.

Li, Y.P., Zhu, X.F., Zhang, G.P., Tan, J., Wang, W., Wu, B., 2010b. Investigation of deformation instability of Au/Cu multilayers by indentation. Philos. Mag. A 90, 3049–3067.

Liang, C., Zhang, Q., Shao, Y., Bu, Y., Liu, J., Li, X., Wang, H., Yang, W., 2021. Influence of load orientations with respect to twin boundaries on the deformation behaviors of high-entropy alloy nanocrystals. MRS Bull. 46, 205–216.

Liu, R., Tang, J., Jiang, J., Li, X., Wei, Y., 2022. Stacking fault induced hardening and grain size effect in nanocrystalline CoNiCrFeMn high-entropy alloy. Extreme Mechanics Letters 56, 101875.

Liu, Y., Bufford, D., Wang, H., Sun, C., Zhang, X., 2011. Mechanical properties of highly textured Cu/Ni multilayers. Acta Mater. 59, 1924–1933.

Liu, Y., Chen, Y., Yu, K.Y., Wang, H., Chen, J., Zhang, X., 2013. Stacking fault and partial dislocation dominated strengthening mechanisms in highly textured Cu/Co multilayers. Int. J. Plast. 49, 152–163.

Lu, L., Chen, X., Huang, X., Lu, K., 2009. Revealing the maximum strength in nanotwinned copper. Science 323, 607–610.

Mara, N.A., Bhattacharyya, D., Dickerson, P., Hoagland, R.G., Misra, A., 2008. Deformability of ultrahigh strength 5nm Cu/Nb nanolayered composites. Appl. Phys. Lett. 92, 231901.

Miracle, D.B., Senkov, O.N., 2017. A critical review of high entropy alloys and related concepts. Acta Mater. 122, 448–511.

Misra, A., Verdier, M., Lu, Y.C., Kung, H., Mitchell, T.E., Nastasi, M., Embury, J.D., 1998. Structure and mechanical properties of Cu-X (X = Nb,Cr,Ni) nanolayered composites. Scripta Mater. 39, 555–560.

Misra, A., Kung, H., Hammon, D., Hoagland, R.G., Nastasi, M., 2003. Damage mechanisms in nanolayered metallic composites. Int. J. Damage Mech. 12, 365–376.

Misra, A., Hirth, J.P., Hoagland, R.G., 2005a. Length-scale-dependent deformation mechanisms in incoherent metallic multilayered composites. Acta Mater. 53, 4817–4824.

Misra, A., Zhang, X., Hammon, D., Hoagland, R.G., 2005b. Work hardening in rolled nanolayered metallic composites. Acta Mater. 53, 221–226.

Misra, A., Hirth, J.P., Hoagland, R.G., Embury, J.D., Kung, H., 2004. Dislocation mechanisms and symmetric slip in rolled nano-scale metallic multilayers. Acta Mater. 52, 2387–2394.

Misra, A., Hoagland, R.G., 2007. Plastic flow stability of metallic nanolaminate composites. J. Mater. Sci. 42, 1765–1771.

Mompiou, F., Caillard, D., Legros, M., Mughrabi, H., 2012. In situ TEM observations of reverse dislocation motion upon unloading in tensile-deformed UFG aluminium. Acta Mater. 60, 3402–3414.

Nasim, M., Li, Y., Wen, M., Wen, C., 2019. High-strength Ni/Al nanolaminates fabricated by magnetron sputtering and their nanoindentation and nanowear behaviors. Materialia 6, 100263.

Nasim, M., Li, Y.C., Wen, M., Wen, C.E., 2020. A review of high-strength nanolaminates and evaluation of their properties. J. Mater. Sci. Technol. 50, 215–244.

Niu, J.J., Zhang, J.Y., Liu, G., Zhang, P., Lei, S.Y., Zhang, G.J., Sun, J., 2012. Size-dependent deformation mechanisms and strain-rate sensitivity in nanostructured Cu/X (X=Cr, Zr) multilayer films. Acta Mater. 60, 3677–3689.

Pacchioni, G., 2022. High-entropy materials go nano. Nat. Rev. Mater. 7, 156, 156.

Qin, F., Lu, W.J., Li, J.J., 2022. Enhanced resistance to shear instability by gradient nanolayered structures in sputtered Cu/Zr composites. Mater. Sci. Eng., A 846, 143253.

Qin, F., Chen, F., Hou, J., Lu, W., Chen, S., Li, J., 2024. Strong resistance to shear instability in multilayered metallic composites by nanoscale amorphous-BCC crystalline interfaces. Mater. Sci. Eng., A 891, 145919.

Schneider, M., George, E.P., Manescau, T.J., Záležák, T., Hunfeld, J., Dlouhý, A., Eggeler, G., Laplanche, G., 2020. Analysis of strengthening due to grain boundaries and annealing twin boundaries in the CrCoNi medium-entropy alloy. Int. J. Plast. 124, 155–169.

Sohn, S.S., Kwiatkowski da Silva, A., Ikeda, Y., Körmann, F., Lu, W., Choi, W.S., Gault, B., Ponge, D., Neugebauer, J., Raabe, D., 2019. Ultrastrong medium-entropy single-phase alloys designed via severe lattice distortion. Adv. Mater. 31, 1807142.

Su, R., Neffati, D., Li, Q., Xue, S., Fan, C., Cho, J., Zhang, Y., Li, J., Wang, H., Kulkarni, Y., Zhang, X., 2021. Ultra-high strength and plasticity mediated by partial dislocations and defect networks: Part II: layer thickness effect. Acta Mater. 204, 116494.

Wang, J., Hoagland, R.G., Liu, X.Y., Misra, A., 2011. The influence of interface shear strength on the glide dislocation–interface interactions. Acta Mater. 59, 3164–3173.

Wen, S.P., Zong, R.L., Zeng, F., Gao, Y., Pan, F., 2007. Evaluating modulus and hardness enhancement in evaporated Cu/W multilayers. Acta Mater. 55, 345–351.

Wu, S.H., Cheng, P.M., Wu, K., Hou, Z.Q., Wang, Y.Q., Liang, X.Q., Li, J., Kuang, J., Zhang, J.Y., Liu, G., Sun, J., 2018. Effect of He-irradiation fluence on the size-dependent hardening and deformation of nanostructured Mo/Zr multilayers. Int. J. Plast. 111, 36–52.

Ye, Y.F., Wang, Q., Lu, J., Liu, C.T., Yang, Y., 2016. High-entropy alloy: challenges and prospects. Mater. Today 19, 349–362.

Yu, K.Y., Liu, Y., Rios, S., Wang, H., Zhang, X., 2013. Strengthening mechanisms of Ag/Ni immiscible multilayers with fcc/fcc interface. Surf. Coating. Technol. 237, 269–275.

Zeng, Y., Li, X., 2021. Atomistic simulations of high-temperature creep in nanotwinned TiAl alloys. Extreme Mechanics Letters 44, 101253.

Zhang, G.P., Liu, Y., Wang, W., Tan, J., 2006. Experimental evidence of plastic deformation instability in nanoscale Au/Cu multilayers. Appl. Phys. Lett. 88.

Zhang, J.Y., Lei, S., Niu, J., Liu, Y., Liu, G., Zhang, X., Sun, J., 2012. Intrinsic and extrinsic size effects on deformation in nanolayered Cu/Zr micropillars: from bulk-like to small-volume materials behavior. Acta Mater. 60, 4054–4064.

Zhang, J.Y., Liu, G., Sun, J., 2014. Self-toughening crystalline Cu/amorphous Cu–Zr nanolaminates: deformation-induced devitrification. Acta Mater. 66, 22–31.

Zhang, J.Y., Zeng, F.L., Wu, K., Wang, Y.Q., Liang, X.Q., Liu, G., Zhang, G.J., Sun, J., 2016. Size-dependent plastic deformation characteristics in He-irradiated nanostructured Cu/Mo multilayers: competition between dislocation-boundary and dislocation-bubble interactions. Mater. Sci. Eng., A 673, 530–540.

Zhang, Q., Huang, R., Jiang, J., Cao, T., Zeng, Y., Li, J., Xue, Y., Li, X., 2022. Size effects and plastic deformation mechanisms in single-crystalline CoCrFeNi micro/nanopillars. J. Mech. Phys. Solid. 162, 104853.

Zhang, Q., Niu, R., Liu, Y., Jiang, J., Xu, F., Zhang, X., Cairney, J.M., An, X., Liao, X., Gao, H., Li, X., 2023. Room-temperature super-elongation in high-entropy alloy nanopillars. Nat. Commun. 14, 7469.

Zhang, R.F., Wang, J., Beyerlein, I.J., Germann, T.C., 2011. Dislocation nucleation mechanisms from fcc/bcc incoherent interfaces. Scripta Mater. 65, 1022–1025.

Zhang, X., Misra, A., Wang, H., Shen, T.D., Swadener, J.G., Embury, J.D., Kung, H., Hoagland, R.G., Nastasi, M., 2003. Strengthening mechanisms in nanostructured copper/304 stainless steel multilayers. J. Mater. Res. 18, 1600–1606.

Zhang, X., Misra, A., Wang, H., Shen, T.D., Nastasi, M., Mitchell, T.E., Hirth, J.P., Hoagland, R.G., Embury, J.D., 2004. Enhanced ardening in Cu/330 stainless steel multilayers by nanoscale twinning. Acta Mater. 52, 995–1002.

Zhao, Y., Zhang, J., Wang, Y., Wu, S., Liang, X., Wu, K., Liu, G., Sun, J., 2021. The metastable constituent effects on size-dependent deformation behavior of nanolaminated micropillars: Cu/FeCoCrNi vs Cu/CuZr. J. Mater. Sci. Technol. 68, 16–29.

Zhao, Y.F., Wang, Y.Q., Wu, K., Zhang, J.Y., Liu, G., Sun, J., 2018. Unique mechanical properties of Cu/(NbMoTaW) nanolaminates. Scripta Mater. 154, 154–158.

Zhao, Y.F., Zhang, J.Y., Wang, Y.Q., Wu, K., Liu, G., Sun, J., 2019. Unusual plastic deformation behavior of nanotwinned Cu/high entropy alloy FeCoCrNi nanolaminates. Nanoscale 11, 11340–11350.

Zhao, Y.F., Zhang, J.Y., Wang, Y.Q., Wu, K., Liu, G., Sun, J., 2020. Size-dependent mechanical properties and deformation mechanisms in Cu/NbMoTaW nanolaminates. Sci. China Mater. 63, 444–452.

Zhao, Y.F., Chen, H.H., Zhang, D.D., Zhang, J.Y., Wang, Y.Q., Wu, K., Liu, G., Sun, J., 2022. Unusual He-ion irradiation strengthening and inverse layer thickness-dependent strain rate sensitivity in transformable high-entropy alloy/metal nanolaminates: a comparison of Fe50Mn30Co10Cr10/Cu vs Fe50Mn30Co10Ni10/Cu. J. Mater. Sci. Technol. 116, 199–213.

Zheng, S.J., Beyerlein, I.J., Carpenter, J.S., Kang, K., Wang, J., Han, W., Mara, N.A., 2013. High-strength and thermally stable bulk nanolayered composites due to twin-induced interfaces. Nat. Commun. 4, 1696.

Zheng, S.J., Wang, J., Carpenter, J.S., Mook, W.M., Dickerson, P.O., Mara, N.A., Beyerlein, I.J., 2014. Plastic instability mechanisms in bimetallic nanolayered composites. Acta Mater. 79, 282–291.

Zou, Y., Ma, H., Spolenak, R., 2015. Ultrastrong ductile and stable high-entropy alloys at small scales. Nat. Commun. 6, 7748.